Transactions in GIS

WILEY

Transactions in GIS

RESEARCH ARTICLE OPEN ACCESS

Prediction of LAI in Scots Pine Forests of Türkiye Using UAV and Sentinel 2 Images

Hasan Aksoy[1,2] | Annika Kangas[2] | Petteri Packalen[3] | Lauri Korhonen[4] | Alkan Günlü[5]

[1]Department of Forestry, Program of Forestry and Forest Products, Vocational School of Ayancık, Sinop University, Sinop, Türkiye | [2]Natural Resources Institute Finland (LUKE), Joensuu, Finland | [3]Natural Resources Institute Finland (LUKE), Helsinki, Finland | [4]School of Forest Sciences, University of Eastern Finland, Joensuu, Finland | [5]Department of Forestry Engineering, Faculty of Forestry, Çankırı Karatekin University, Çankırı, Türkiye

Correspondence: Hasan Aksoy (haksoy@sinop.edu.tr)

Received: 27 December 2025 | **Revised:** 22 April 2026 | **Accepted:** 7 May 2026

Keywords: LAI | random forest | sentinel 2 | temperate forest | UAV

ABSTRACT

Monitoring the structural characteristics of vegetation cover is critical for understanding ecosystem functioning and sustainable forest management. Effective Leaf area index (LAIe) is directly related to photosynthetic capacity, carbon cycle, and water balance of ecosystems. In this study, LAIe prediction was performed using random forest algorithms with five different datasets obtained from unmanned aerial vehicle (UAV) images and Sentinel 2 (S2) satellite images. The study aimed to (1) determine which UAV features perform best in the prediction of LAIe, and (2) to compare prediction accuracies obtained while using UAV and S2 features. To evaluate the contribution of different data sources, five datasets were considered, namely UAV_RGB (DS1), UAV_3D (DS2), UAV_ALL (DS3), S2 (DS4), and ALL (DS5), with corresponding RMSE% values of approximately 27.3, 29.6, 24.4, 32.1, and 24.8, respectively. The results showed that the DS3 dataset provided the highest accuracy and the most balanced error distribution. The DS5 resulted in more stable prediction performance compared to individual datasets, enabling the model to demonstrate similar accuracy levels for both low and high LAIe values. We conclude that low-cost UAV-RGB data, utilizing both 3D and 2D features, is an effective alternative to high-cost remote sensing techniques for LAIe prediction.

1 | Introduction

Leaf Area Index (LAI) is one of the essential biophysical parameters used to understand structural and functional characteristics of forest ecosystems. Defined by Chen and Black (1992) as "half of the total leaf area per unit horizontal surface area," LAI directly affects the photosynthetic capacity, carbon cycle, evapotranspiration processes, and water-energy balances of ecosystems (Chen and Black 1992; Bréda 2003). Therefore, LAI is considered an indispensable component of both process-based ecosystem models and sustainable forest management practices. The Global Climate Observing System (Zhang et al. 2024) has identified LAI as one of the mandatory core variables for monitoring climate change. Furthermore, LAI is included in the list of core biodiversity variables developed under the Convention on Biological Diversity as an indicator of ecosystem structure and function (Skidmore et al. 2021).

Accurate LAI prediction is important for determining the carbon absorption capacity of forest ecosystems (Running and Coughlan 1988), understanding rainfall retention and the water cycle (Gower and Norman 1991), monitoring forest health (Chen and Cihlar 1996), and modeling energy balance (Sellers et al. 1997). However, measuring LAI is not always easy. Although direct methods (e.g., leaf collection and area measurement) provide the most accurate results, such destructive methods are time consuming, making them impractical for large areas (Gower et al. 1999). Indirect methods, such as hemispherical photographs or the LAI-2000 Plant Canopy Analyzer, are more practical and therefore commonly used (Welles and Norman 1991). However, indirect methods are sensitive to factors such as shading, leaf angle distribution, and the presence of woody components, and they often produce systematic errors due to the clumping effect (Nilson 1971; Chen and Black 1992; Garrigues et al. 2008; Liu et al. 2015).

The limitations of field based LAI measurement methods have encouraged the use of remote sensing technologies. Field measured LAI has been correlated with spectral indices derived from UAV, airborne, and satellite sensors, as well as with 3D structural characteristics and their combinations (Jensen et al. 2008; Richardson et al. 2009; Pope and Treitz 2013; Heiskanen et al. 2015; Qu et al. 2018). Passive optical sensors, particularly MODIS (Myneni et al. 1997) and S2, enable production of large-scale LAI maps. However, such passive systems are affected by cloud cover and spectral saturation. As a result, accuracy levels tend to decrease as forest cover increases (Fang et al. 2008). These limitations of passive sensors are largely overcome by the ability of Airborne Lidar Scanning (ALS) to reveal the three-dimensional structure of forests with high accuracy (Lidar 2002). However, due to the cost and operational limitations of ALS, inexpensive photogrammetric data produced with RGB sensors offer a practical alternative for forestry research (Wallace et al. 2016; Puliti et al. 2020; Hartley et al. 2025). This cost advantage allows for repeated flights and efficient monitoring of changes in LAI. Many kinds of models can be employed for the prediction of LAI from remote sensing data. These models include parametric linear models (Schlerf et al. 2005; Günlü et al. 2017; Meyer et al. 2019), artificial neural networks (Xie et al. 2021), random forests (RF) (Bhattarai et al. 2022), support vector machines (Verrelst et al. 2011; Omer et al. 2016), partial least squares regression (Vafaei et al. 2021), and gradient boosted trees (Zhao et al. 2023). Especially the RF method is frequently used due to its robustness against overfitting, ability to evaluate feature importances, and insensitivity to hyperparameter optimization.

Lin et al. (2021) predicted LAI using features obtained from multi angle images acquired with a multispectral UAV sensor (RMSE ≈0.65). Zhang et al. (2023) used a hyperspectral UAV sensor (RMSE ≈0.20). In a study by Zhang et al. (2024), LAI was estimated using ALS data with semi physical and empirical models (RMSE ≈0.26–0.05). The literature indicates that UAV based methods for LAI prediction primarily utilize high cost LIDAR, hyperspectral, and multispectral sensors. Therefore, one of the biggest gaps in the literature is the extent to which LAI predictions can be achieved using inexpensive RGB cameras, which are more accessible to many practitioners. The feasibility of using RGB sensor-equipped UAVs as a practical and economical solution for LAI prediction therefore needs to be investigated. Additionally, some sources indicate that low-cost RGB camera in a UAVprovides more reliable and balanced data for LAI predictions compared to open satellite-based data (Lin et al. 2021). Studies directly comparing LAI estimates based on satellite and RGB sensor equipped UAVs and focusing on optimizing their concurrent use are limited, and multi-source data integration remains an important area requiring investigation. Furthermore, UAV based methods have not been tested systematically enough in different forest types. Most studies focus on a specific species or region, which makes it difficult to obtain generalizable LAI results (Zhang et al. 2024).

The general aim of this study was to predict LAIe using data obtained from UAV based RGB and S2 images in pure Scots pine forests located in mountainous areas of Türkiye. Two different datasets were created from RGB data: one consisting of spectral features, and the other consisting of point cloud features. Furthermore, LAIe was predicted using features obtained only from S2. The final aim of the study was to investigate the role of dataset combinations in LAIe prediction.

2 | Material and Method

2.1 | Material

2.1.1 | Study Area

This study was conducted in the mountain forests of Sinop Province, located in the northernmost part of Türkiye. The study area has an average annual rainfall of 685.7 mm and a temperature of 14°C. The highest rainfall is observed in October, while the lowest rainfall is observed in May. The region is characterized by rich and diverse forest cover thanks to regular rainfall throughout the year. The elevation levels range from 100 to 1200 m with variable slopes. While humid microclimate conditions prevail on the northern slopes, a drier environmental structure is observed on the southern slopes. This topographic and climatic diversity shapes the distribution of species and the structure of the forest ecosystem. Distinctly different coniferous and broadleaf tree species are prevalent in the study area. The main tree species include Anatolian black pine (*Pinus nigra*), Scots pine (*Pinus sylvestris*), oriental spruce (*Picea orientalis*), fir (*Abies nordmanniana*), oriental beech (*Fagus orientalis*), oak species (*Quercus* spp.), and ash (*Fraxinus excelsior*) (GDF 2022). The location of the study area is shown in Figure 1.

2.1.2 | Field LAI, Satellite and UAV Data

In this study, effective leaf area index (LAIe) reference data were obtained from 172 circular sample plots using hemispherical photography. The study considered different stages of growth: 8 cm–19.9 cm (Young), 20 cm–35.9 cm (Middle-age), and ≥ 36 cm (Old), as well as crown closure rates ((1) 11%–40%, (2) 41%–70%, and (3) 71%–100%) (GDF 2022), and different site classes. Accordingly, LAIe measurements were carried out on 172 circular sample plots. The sizes of the sample plots were established based on stand density: 400 m^2 for fully closed stands (3), 600 m^2 for moderately closed stands (2), and 800 m^2 for sparsely closed stands (1). By establishing sample plots in this way, the aim was to create a representative sample from Scots pine stands, thereby including trees from different age, diameter, and crown closure classes. In these plots, with radii ranging from 11.28 to 15.96 m, 180° hemispherical images facing the canopy were obtained at a height of approximately 1.5 m above the ground using a Canon EOS 50D camera and a Sigma 8 mm fisheye lens. In each plot, images were captured from 5–7 different points at four different locations extending from the center to the plot boundary (Aksoy 2022). A total of 1030 images were obtained. These images, acquired under conditions avoiding direct sunlight, were analyzed

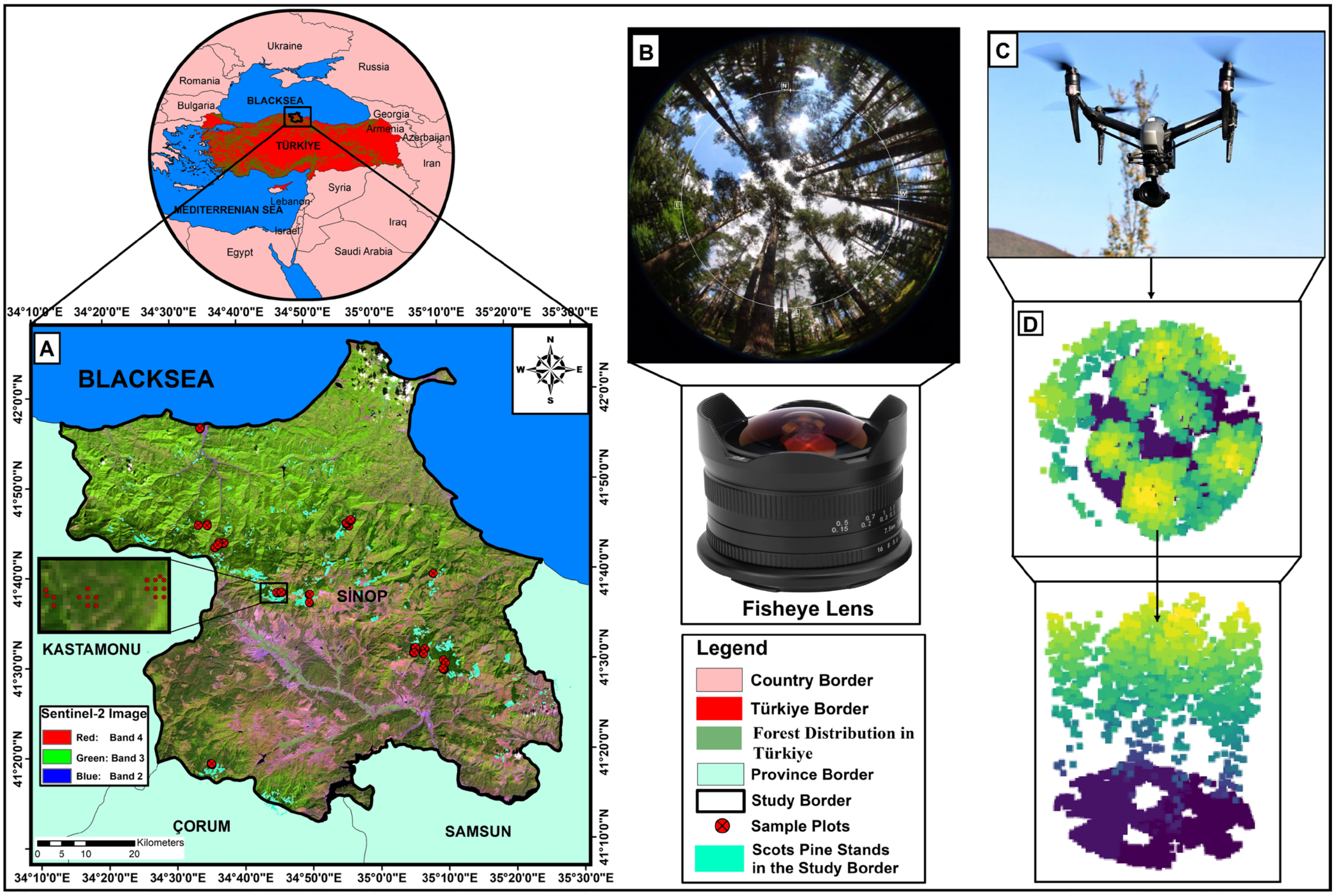

FIGURE 1 | Map of the study area. (A) S2 image of the study area boundary, (B) Taking of field images for LAIe, (C) UAV used in the study, (D) Sample plot SfM-derived point cloud view.

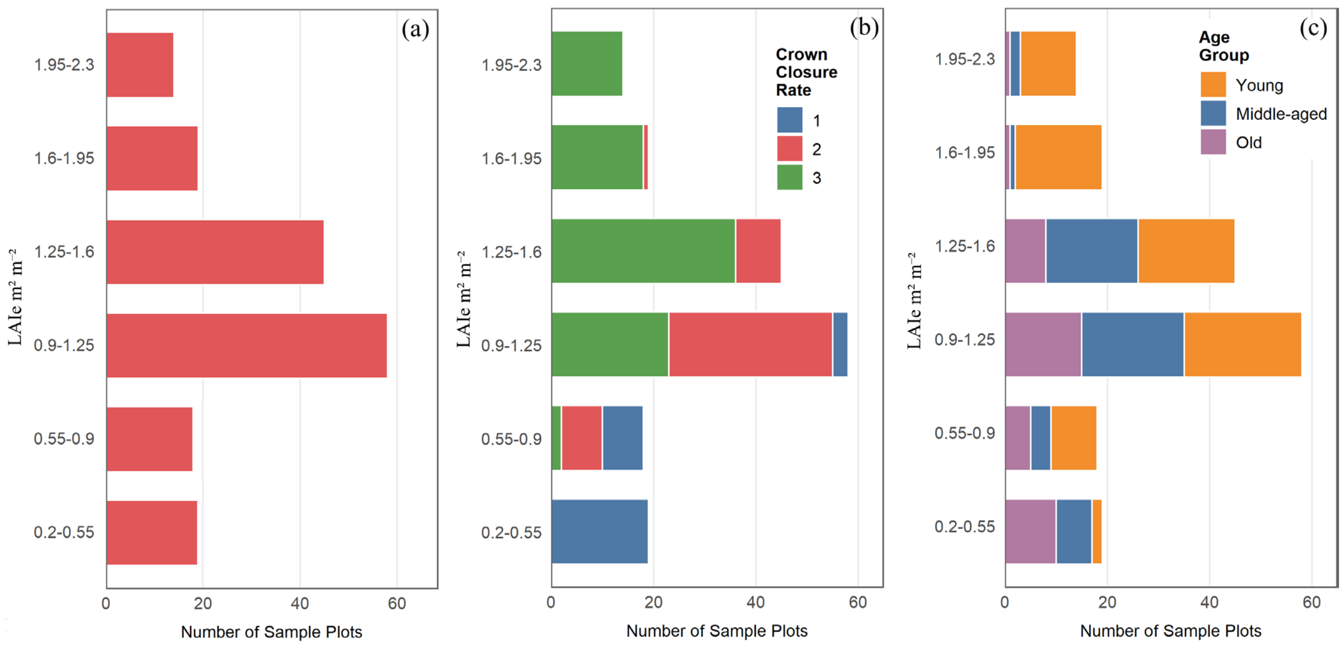

FIGURE 2 | Distribution of the LAIe values by number of sample plots, diameter classes, and canopy cover rate. (a) Distribution of LAIe according to the number of sample plots in the study area, (b) Distribution of LAIe according to crown closure rate (1, 2, and 3), and (c) Distribution of LAIe according to breast-height diameter classes (Young, Middle-age, and Old) based on the number of sample plots in the study area.

and used as field-based LAIe data. The descriptive statistics of the LAIe values for the study area were minimum $0.25\,m^2\,m^{-2}$, maximum $2.30\,m^2\,m^{-2}$, mean $1.20\,m^2\,m^{-2}$, median $1.21\,m^2\,m^{-2}$, standard deviation $0.42\,m^2\,m^{-2}$, and variance $0.18\,m^2\,m^{-2}$. In addition, the distribution of LAIe values in the study area, based on sample plots, is presented in Figure 2.

TABLE 1 | Descriptive characteristics related to UAV, S2, and GNSS.

DJI Zenmuse X-5S camera specification	
20.8 MP still image capture	
12.8-stop dynamic range	
12-bit raw photos	
9 mm–45 mm Objective Length	
4/3” CMOS sensor (~17.3 × 13.0 mm)	
Gezgin 1 GNSS specification	
Supported Signals	GPS L1/L2/L5, GLONASS L1/L2, BDS B1/B2/B3
Single Point Positioning (RMS)	Horizontal: 1.5 m, Vertical: 2.5 m
Differential GNSS/DGNSS (RMS)	Horizontal: 0.4 m, Vertical: 0.8 m
Network RTK/CORS (RMS)	Horizontal: 1 cm + 1 ppm, Vertical: 1.5 cm + 1 ppm
Correction Data Formats	RTCM 2.3/3.0/3.2
Identifying specifications of UAV images	
Parameter	**Value**
Average Ground Sampling Distance (GSD)	2.87 cm
Median Matched Keypoints per Image	2302
Dense Point Cloud Points	14,080,391 points
Average Point Density	73.64 points/m^3
Overlap	> 5 images per pixel across most of the area
Ground Control Points (GCPs)	1 GCP: Error X = 0.63 m, Y = 0.364 m, Z = 0.846 m
Absolute Geolocation RMS Error	X = 0.88 m, Y = 0.67 m, Z = 0.97 m
DSM & Orthomosaic Resolution	1 × GSD (2.87 cm/pixel)
DTM Resolution	5 × GSD (14.35 cm/pixel)

S2 specification			
Chanel	**Spectral range**	**Wavelength range (μm)**	**Spatial resolution (m)**
B2	Blue (B)	458–523	10
B3	Green (G)	543–578	10
B4	Red (R)	650–680	10
B5	Red Edge 1	698–713	20
B6	Red Edge 2	733–748	20
B7	Near Infrared 1 (NIRNarrow 1)	773–793	20
B8	Near Infrared (NIR)	785–900	10
B8A	Near Infrared 2 (NIRNarrow 2)	855–875	20
B11	Shortwave Infrared (SWIR 1)	1565–1655	20
B12	Shortwave Infrared (SWIR 2)	2100–2280	20

The S2(L1C) satellite image was acquired in September 2022. Four of the relevant bands have a spatial resolution of 10 m (B2, B3, B4, B8) and six have a spatial resolution of 20 m (B5, B6, B7, B8A, B11, B12) (Table 1). The radiometric resolution is 12 bits, and the swath width is 290 km (ESA 2022). The UAV data used in the study were obtained using the Zenmuse X5 RGB camera integrated into the DJI Inspire 2 UAV (Table 1) (Aksoy and Günlü 2025a). A total of 1224 images were taken during the eleven flights planned to cover each sample plot. All flights were conducted at an altitude of 120 m above ground level, with an overlap rate of 80% in the forward direction and 70% in the lateral direction, and the camera was fixed at a 90° (nadir)

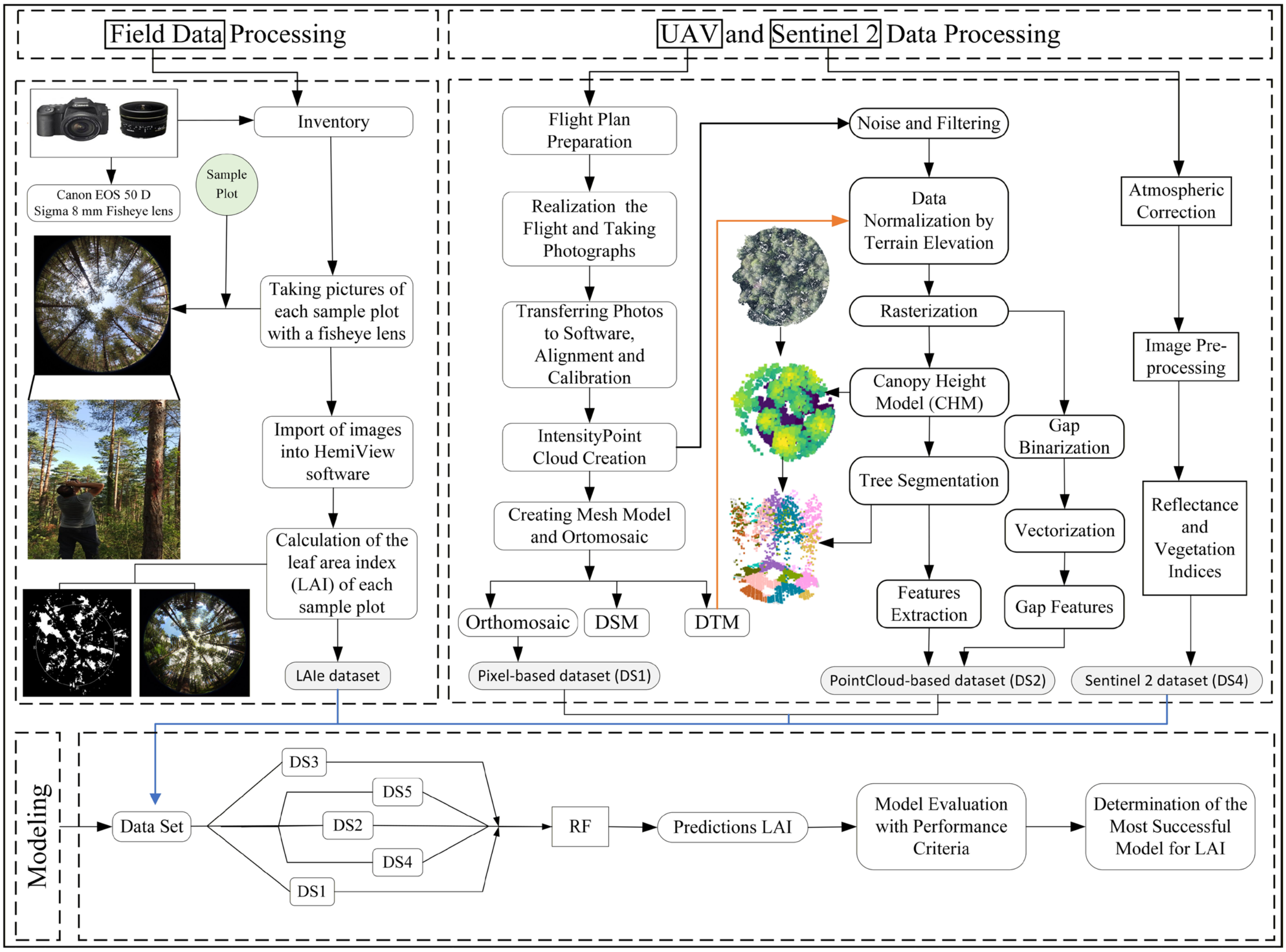

FIGURE 3 | General workflow chart of the study.

position. All flights were conducted in the same year as the field measurements (September 2022). Additionally, ground control points (GCPs) were established to increase positional accuracy. Gezgin 1 GNSS device was used to obtain the center coordinates of the sample plots with the GPCs. The technical specifications of the Gezgin 1 are presented in Table 1. The images obtained were processed using Pix4D software to generate orthomosaics, Digital Surface Models (DSM), Digital Terrain Models (DTM), and point cloud data for the sample plots.

2.2 | Method

The study was conducted in three main stages. The first stage involved LAIe measurement and calculations using hemispherical photographs. The second stage involved processing data from UAV and S2 and deriving modeling inputs. Finally, the third stage involved modeling and performance evaluation processes using RF. Within this context, five datasets were created for LAIe estimation. These are DS1, UAV orthomosaic derived spectral features (2D raster); DS2, UAV SfM-derived 3D structural metrics; DS3, a combination of DS1 and DS2; DS4, S2 derived spectral features; and finally, DS5, a dataset obtained by combining the previous four datasets. The detailed workflow is presented schematically in Figure 3.

2.2.1 | Preparation of the LAIe Data Set

Ground LAIe data were calculated by analyzing hemispherical photographs obtained from each sample plot using the HemiView v2.1 SR4 software. HemiView evaluates gap fraction values using an inverse solution approach and estimates both LAIe and the leaf orientation parameter (ELADP) with a theoretical hemispherical canopy model (Delta-T Devices). Assuming that the leaf orientation distribution may be represented as random, vertically weighted (erectile), or horizontally weighted (planophile), the G(θ) projection coefficient was calculated within the HemiView framework and LAIe values were estimated using Equation (1). Within the HemiView framework, LAIe values were estimated by inverting the gap fractions derived from hemispherical photographs. In coniferous stands such as Scots pine, the angular distribution involved in this process should not only be interpreted as needle orientation, but also as the overall orientation of visible plant elements within the canopy. The response variable used in this study corresponds to LAIe rather than clumping-corrected true LAIe because no explicit clumping correction was applied. This distinction is particularly relevant in coniferous canopies, where clumping at shoot and canopy levels may cause optical methods to underestimate the actual LAIe. In line with the study's objectives, LAIe was considered an appropriate reference variable.

However, when interpreting the results, uncertainty related to foliage aggregation and the structural complexity of Scots pine canopies should be acknowledged. Following this approach, the photographs obtained for each sample plot were analyzed individually in HemiView.

$$LAIe = \frac{\ln(P(\theta)) \times \cos(\theta)}{G(\theta)} \tag{1}$$

where $P(\theta)$: Gap fraction, $G(\theta)$: Geometric factor expressing leaf orientation distribution and θ: Zenith angle.

Within the HemiView framework, canopy gap fractions derived from hemispherical photographs were used to estimate LAIe. Since no explicit clumping correction was applied in this study, the response variable used does not represent clumping corrected true LAI, but rather LAIe. In this context, the influence of needle clumping, woody components (stems and branches), thresholding, and the spatial heterogeneity of plant elements should be regarded as sources of uncertainty inherent to the optical measurement process. Therefore, the resulting LAIe values were used as the reference variable in the modeling process. The observed variation in LAIe values within the range of 0.25–2.30 is considered to be closely related to the heterogeneous stand structure of the study area. In particular, the presence of young, old, and low-canopy-cover stands is likely to have contributed to the relatively low and moderate LAIe values observed in the dataset. Indeed, it is well known that canopy leaf area tends to be lower in young, sparse, and structurally open stands (Bréda 2003). As shown in Figure 2, a substantial proportion of the sample plots are concentrated in the low and medium LAIe ranges, which appears to be consistent with the age class and crown closure distribution of the study area.

2.2.2 | UAV and S2 Image Processing and Feature Extraction

The UAV images were processed using Pix4D software in three main stages to create orthomosaics, DSM, DTM, and point cloud data. In the first stage, the UAV images were imported into Pix4D software, and the initial camera optimization was performed (Aksoy and Günlü 2025b). Automatic control points were generated by the software, and GCPs measured in the field were manually marked on all images. As a result of this process, the image block was geographically referenced with high accuracy in the X, Y, and Z directions. Statistical results regarding GCP accuracy are presented in Table 1.

In the second stage, a dense point cloud was created using the Structure from Motion (SfM) and Multi-View Stereo (MVS) workflow. During the SfM process, key points were detected using the Scale-Invariant Feature Transform algorithm, and both the interior and exterior camera orientations were optimized through bundle adjustment (Niederheiser et al. 2016). In the MVS process, a hybrid approach combining Semi Global Matching (SGM) and Patch-based Multi View Stereo (PMVS) methods was used. SGM optimizes pixel correspondences between multiple images to produce reliable depth maps on low-textured surfaces (Pix4D 2024). The PMVS method enables the acquisition of more detailed point clouds by matching image patches to reconstruct detailed 3D structures in areas with complex surface morphology (Shao et al. 2016). Optimal density and multi-scale parameters were chosen to balance detail preservation and processing efficiency. After creating a dense point cloud, statistical outlier removal was applied to filter inconsistent points caused by moving objects, reflections, or sky regions.

In the final stage, the point cloud was classified into ground and non-ground points. Ground points were used to create the DTM, while the entire point cloud was used to create the DSM. Finally, images were orthorectified to the DTM, and band digital values (DN), band reflectance values, vegetation indices, and other derived features were calculated for the DS1 (Table 2).

The second dataset DS2 consists of features SfM-derived 3D data. SfM-derived 3D data processing and feature extraction were performed using the R programming language (R Core Team 2016) with the 'lidR' (Roussel et al. 2018), 'raster' (Hijmans 2018), and 'sp' (Pebesma and Bivand 2005) packages. First, the 3D data was normalized relative to terrain elevation. During this process, the height of each point was recalculated based on its elevation above the terrain surface. Additionally, height values identified as outliers were filtered to reduce noise and improve model accuracy. Next, the normalized 3D data was interpolated into raster format for Canopy Height Model (CHM) production, and vegetation heights were calculated using the point to raster method. Median filtering was applied to the CHM to reduce spatial noise, thereby ensuring a more accurate representation of tree crown morphology. In the next step, a local maximum based tree top detection algorithm was applied to the CHM with a dynamic window size (Figure 4). The detected tops were used as inputs to the tree segmentation algorithm developed by Dalponte and Coomes (2016). Thus, point cloud segments corresponding to each tree were separated, and CHM based features such as heights and densities were calculated to create a feature set at the sample parcel level (Table 3).

Afterwards, gap features were derived to evaluate the gap structure in the forest canopy. Gap areas were determined using a height threshold-based classification approach with CHM derived from normalized point cloud data. In this context, pixels below a certain elevation threshold (<2 m) were defined as canopy gaps. Gap features such as the total gap area percentage (%Gap), mean gap size, gap count, and gap area distribution were calculated for each sample plot. These features were calculated using the "chm_layer_metrics" and "lasmetrics" functions in the lidR package. Then, the morphological characteristics of the gap pixels were extracted using the raster zonal statistics method. All these features obtained in this context (Table 3) were collected in a SfM-derived 3D data named DS2 and prepared for use in the modeling process.

The satellite predictors were obtained from a L1C (Top of Atmosphere, TOA) S2 imagery. Since access to L2A (Bottom-of-Atmosphere, BOA) products was limited for some dates during the study period, L1C imagery was used instead. Atmospheric correction was then performed with the Semi-Automatic Classification Plugin (SCP) included in the QGIS 3.8.1 software. The SCP plugin integrates Sen2Cor-based atmospheric

TABLE 2 | Formulas of vegetation indices and features obtained from UAV images.

Vegetation indices	Formulas	References
RGBVI (Red (R), Green (G) and Blue (B) Vegetation Index)	$(G \times G) - (R \times B) / (G \times G) + (R \times B)$	Bendig et al. (2015)
GLI (Green Leaf Index)	$(2 \times G - R - B) / (2 \times G + R + B)$	Louhaichi et al. (2001)
VARI (Visible Atmospherically Resistant Index)	$(G - R) / (G + R - B)$	Gitelson et al. (2002)
NGRDI (Normalized Green Red Difference Index)	$(G - R) / (G + R)$	C. J. Tucker (1979)
ERGBVE (Enhanced RGB Vegetation Index)	$\pi \times ((G2 - (R \times B)) / (G2 + (R \times B))$	Themistocleous (2019)
GR (Simple red–green ratio)	R / G	Gamon and Surfus (1999)
RGBVI2 (RGB-based vegetation index 2)	$(G - R) / B$	García-Fernández et al. (2021)
TGI (Triangular Greenness Index)	$G - 0.39 \times R - 0.61 \times B$	Hunt et al. (2013)
GRVI (Green–red vegetation index)	$(G - R) / (G + R)$	C. J. Tucker (1979)
MGRVI (Modified green–red vegetation index)	$(G2 - R2) / (G2 + R2)$	Bendig et al. (2015)
BG12 (Simple blue–green ratio)	B / G	Zarco-Tejada et al. (2005)
VEG (Vegetativen)	$G / (Ra \times B(1 - a)); a = 0.667$	Hague et al. (2006)
EXG (Excess green index)	$2G - R - B$	Woebbecke et al. (1995)
NGBDI (Normalized green-blue difference index)	$(G - B) / (G + B)$	Du and Noguchi (2017)
RGBVI3 (RGB-based vegetation index 3)	$(G + B) / R$	García-Fernández et al. (2021)
Features name	**Formulas**	**Abbreviations**
Mean R/G ratio	$mean(R / G)$	mean_R_G
Mean R/B ratio	$mean(R / B)$	mean_R_B
Mean G/B ratio	$mean(G / B)$	mean_G_B
R/G ratio std. dev.	$sd(R / G)$	sd_R_G
R/B ratio std. dev.	$sd(R / B)$	sd_R_B
G/B ratio std. dev.	$sd(G / B)$	sd_G_B
GLI std. dev.	$sd((2G - R - B) / (2G + R + B))$	sdGLI
VARI std. dev.	$sd((G - R) / (G + R - B))$	sdVARI
NGRDI std. dev.	$sd((G - R) / (G + R))$	sdNGRDI
EXG std. dev.	$sd(2G - R - B)$	sdEXG
NGBDI std. dev.	$sd((G - B) / (G + B))$	sdNGBDI
RGB2 std. dev.	$sd((G - R) / B)$	sdRGB2
TGI std. dev.	$sd((G - 0.39) \times (R - 0.61 \times B))$	sdTGI
RGBVI3 std. dev.	$sd((G + B) / R)$	sdRGBVI3
BGI2 std. dev.	$sd(B / G)$	sdBGI2

correction and reflectance calibration processes on S2 L1C data, ensuring the comparability and radiometric consistency of data across different bands (Congedo 2021). Thus, surface reflectance values were calculated for all bands, and atmospheric effects were minimized. The bands obtained after correction (Table 1) were transferred to ArcGIS software and intersected with circular polygons representing each sample plot. The average reflectance values were extracted for the plots using the Zonal Statistics as a Table tool. Then, various vegetation indices were calculated using these values (Table 4). Thus, a DS4 was created by obtaining digital band, reflectance, and vegetation values for each band.

2.2.3 | Modeling and Model Accuracy Evaluation

In this study, LAIe was modeled using RF with five different datasets. RF is a supervized learning-based ensemble algorithm that is frequently used for both classification and regression tasks. The method is based on constructing multiple decision

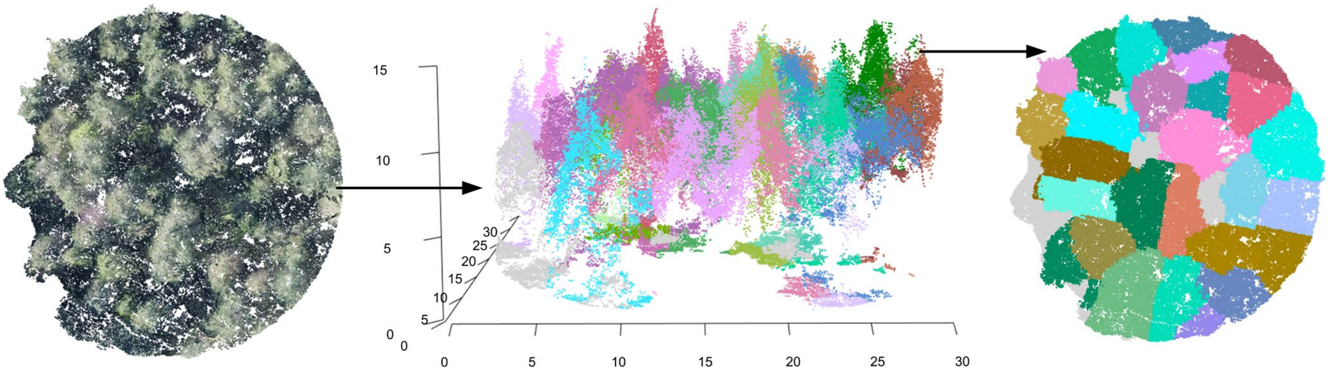

FIGURE 4 | A CHM model created for a sample plot in the study area.

TABLE 3 | Formulas for structural metrics obtained from the SfM-derived 3D data.

Features name	Abbreviations	Formulas
Maximum height	maxZ	$max(Z)$
Mean height	meanZ	$mean(Z)$
90th percentile height	q90Z	$quantile(Z, 0.90)$
75th percentile height	q75Z	$quantile(Z, 0.75)$
Height standard deviation	sdZ	$sd(Z)$
Maximum tree height	maxH	$max(Z)$ $(segmented\ crowns)$
Mean tree height	meanH	$mean(Z)$
Tree height std. dev.	sdH	$sd(Z)$
Number of trees	n_trees	$length(Z)$
Square of number of trees	n_trees_sq	$(length(Z))2$
Mean crown area	mean_crown	$mean(convhull\_area)$
Crown area std. dev.	sd_crown	$sd(convhull\_area)$
Ground percentage	ground_perc	$(sum(Z < 2) / length(Z)) \times 100$
Gap fraction	gap_fraction	$total\_gap\_area / plot\_area$
Gap density	gap_density	$N\_gaps / (plot\_area / 10000)$
Mean gap area	mean_gap_m2	$mean(gap\_area)$
Median gap area	median_gap_m^2	$median(gap\_area)$
Largest gap	largest_gap_m^2	$max(gap\_area)$
90th percentile gap area	p90_gap_m^2	$quantile(gap\_area, 0.9)$
Edge density	edge_density_m_per_ha	$\left(\sum Perimeter / Plot\_Area\right) \times 10000$
Mean shape index	mean_shape_index	$mean(lsm\_p\_shape)$
Mean nearest neighbor distance	mean_nn_m	$mean(NN\_distance)$

trees (Equation 2) and combining the results obtained from these trees (Breiman 2001).

$$\hat{f}(x') = \frac{1}{B} \sum_{b=1}^{B} f_b(x') \tag{2}$$

The RF approach uses data subsets obtained through bootstrapping when constructing each decision tree. During the training of the trees, a randomly selected portion of the variables is included in the model. This mechanism limits the model's overfitting problem and enhances its generalization ability. Thus, the method achieves a high level of accuracy by balancing bias and variance (Liaw and Wiener 2002; Aksoy 2024). One of the most notable advantages of RF is its ability to work effectively with multidimensional data sets and to estimate importances of variables (Equation 3). This process is conducted using observations not included in the model, referred to as out of bag (OOB). The basic idea is to randomly shuffle the values of a specific variable

TABLE 4 | Formulas of vegetation indices obtained from S2.

Vegetation Indices	Formula	References
NDTI	$(B5 - B7)/(B5 + B7)$	Van Deventer et al. (1997)
GDVI	$B5 - B3$	Key and Benson (2006)
SR	$B5/B3$	Birth and McVey (1968)
FII	$(B7/B5)/(B3/B5)$	Kalinowski and Oliver (2004)
GRVI	$(B3 - B4)/(B3 + B4)$	Sripada et al. (2006)
BI	$Sqrt\,(B3 \times B3) + (B4 \times B4)$	Khan et al. (2005)
ND32	$(B4 - B3)/(B4 + B3)$	Lu et al. (2004)
IPVI	$(B5/(B5 + B4))$	Crippen (1990)
ND73	$(B7 - B4)/(B7 + B4)$	Lu et al. (2004)
NDVI	$(B5 - B4)/(B5 + B4)$	Rouse et al. (1974)
NDMI	$(B5 - B6)/(B5 + B6)$	Hardisky et al. (1983)
NBR	$(B5 - B7)/(B5 + B7)$	Key and Benson (2006)
GCI	$B5 - B3 - 1$	Gitelson et al. (2003)
WRI	$(B3 + B4)/(B5 + B7)$	Mukherjee and Samuel (2016)
DVI	$(B5 - B4)$	C. J. Tucker (1980)
NDMI	$(B5 - B6)/(B5 + B6)$	Hardisky et al. (1983)
NDBal	$(B6 - B10)/(B6 + B10)$	Li and Chen (2014)
NBR2	$(B6 - B7)/(B6 + B7)$	DeVries et al. (2016)
SIPI	$(B5 - B3)/(B5 + B4)$	Penuelas et al. (1995)
PSSR	$(B5/B4)$	Blackburn (1998)
ARVI	$(B5 - 2 \times B4) + (B3/B5) + 2 \times (B4) - (B3)$	Kaufman and Tanre (1992)
NDPI	$\left(B5^2\right)/(B5 + B4) \times (B5 + B3)$	Wang et al. (2017)
EVI	$2.5 \times ((B5 - B4)/(B5 + 6 \times B4 - 7.5 \times B2 + 1))$	Liu and Huete (1995)
SAVI	$((B5 - B4)/(B5 + B4 + 0.5)) \times (1.5)$	Huete (1988)
NLI	$\left(B5^2 - B4\right)/\left(B5^2 + B4\right)$	Goel ve Qin (1994)
MSAVI	$(2 \times B5 + 1 - sqrt\,((2 \times B5 + 1)2 - (8 \times (B5 - B4))/2$	Qi et al. (1994)
TCW	$(0.0315 \times B1 + 0.2021 \times B2 + 0.3102 \times B3 + 0.1594 \times B4 - 0.6806 \times B5 - 0.6109 \times B7)$	Frazier et al. (2015)

across OOB samples and then examine the resulting change in model performance. If a significant decrease in accuracy is observed, it is concluded that the variable in question is of greater importance to the model (Janitza and Hornung 2018). RF models were implemented in R (version 4.3.2) using the "randomForest" package (Liaw and Wiener 2002).

$$Importance\left(\mathcal{X}_j\right) = \frac{1}{B}\sum_{b=1}^{B} T_b\left(Accuracy_{OOB}^{(b)} - Accuracy_{OOB\_perm}^{(b)}\right) \quad (3)$$

where $\mathcal{X}_j$: jth independent variable, $Accuracy_{OOB}^{(b)}$: Original accuracy in the OOB dataset, $Accuracy_{OOB\_perm}^{(b)}$: When the jth variable undergoes permutation, accuracy, B: Number of tree.

Each RF model was trained with 500 trees (ntree = 500) and evaluated using 10-fold cross-validation. The mtry value, considered a fundamental hyperparameter in the RF algorithm, was optimized using only the training data. In this context, predefined candidate values for mtry were tested at each training step, and the parameter value yielding the lowest error rate was selected.

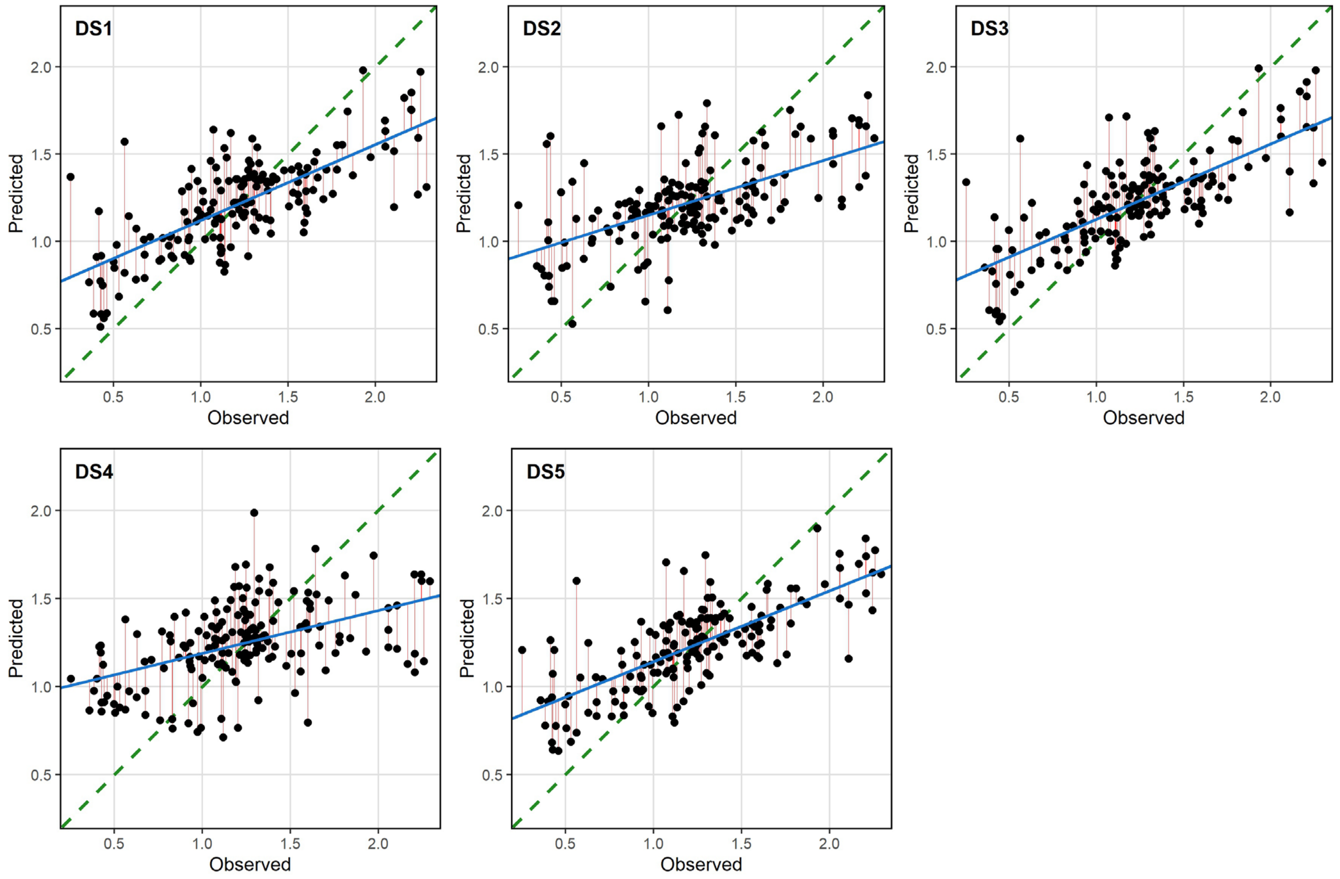

FIGURE 5 | Scatter plots of field measured LAIe and predicted LAIe (DS1-DS5 shows the datasets). The green line in the figure represents the 1:1 line, and the blue line represents the regression line.

To separate hyperparameter selection from performance evaluation, the optimization process was conducted in the inner loop, while the model validation process was carried out in the outer loop (Probst et al. 2019). Thus, performance metrics were calculated using test folds not used in model selection, thereby reducing the risk of data leakage. As a result, the model was rebuilt for each external fold based on the most suitable mtry value, and the final performance metrics were obtained at the end of this process. Furthermore, before applying the RF model, no correlation-based variable selection or separate feature selection was applied to the spectral and structural variables derived from UAV and S2 data, in order to collectively assess their potential contributions to LAIe estimation. The purpose of selecting the RF modeling technique in this study is also to avoid the need for feature selection. This is because this technique is less susceptible to multicollinearity compared to linear modeling approaches and is capable of modeling nonlinear relationships among a large number of explanatory variables. The accuracy was evaluated using the determination coefficient (R^2, Equation 4), root mean square error (RMSE, Equation 5), relative root mean square error (RMSE%, Equation 6), and bias (Bias, Equation 7) criteria.

$$R^2 = 1 - \frac{(n-1)\sum_{i=1}^{n}\left(y_i - \hat{y}_i\right)^2}{(n-p)\sum_{i=1}^{n}\left(y_i - \overline{y}_i\right)^2} \tag{4}$$

$$RMSE = \sqrt{\frac{1}{n}\sum_{i=1}^{n}\left(y_i - \hat{y}_i\right)^2} \tag{5}$$

TABLE 5 | Performance metrics related to LAIe estimation.

Dataset	R^2	RMSE	RMSE%	Bias
DS1	0.44	0.33	27.3	0.004
DS2	0.38	0.36	29.6	0.008
DS3	0.60	0.30	24.4	−0.002
DS4	0.24	0.39	32.1	0.013
DS5	0.57	0.30	24.8	−0.001

$$RMSE\% = \frac{RMSE \times 100\%}{\hat{y}_i} \tag{6}$$

$$Bias = \frac{\sum_{i=1}^{n}\left(y_i - \hat{y}_i\right)}{n} \tag{7}$$

where n is the number of observations, k is the number of coefficients, y_i are measured the stand parameters, $\hat{y}_i$ are predicted stand metrics, $\overline{y_i}$ is a mean of measured stand metrics values, p is the number of parameters.

3 | Results

The LAIe estimation performance was evaluated using five datasets (DS1–DS5) obtained from different data sources. The performance metrics in Table 1 and the scatter plots presented in Figure 4 show the varying accuracy levels depending on the datasets. The DS1 dataset achieved moderate success (R^2 ≈0.44, RMSE ≈0.33) and showed a certain degree of agreement between the observed and predicted values (Figure 4). The DS2 dataset, based on UAV point cloud data, showed similar performance (R^2 ≈0.38, RMSE ≈0.36), but the error values were higher. Graphical analysis (Figure 5) revealed that the predictions in these two datasets showed a linear trend.

The DS3 dataset yielded the most successful result (R^2 ≈0.60, RMS ≈0.30). When examining the results and prediction observation distributions, DS3 stood out with both low error values and high R^2. The scatter plot showed the closest distribution between observed and predicted values (Figure 5).

This result demonstrates that combining different features obtained from UAVs significantly improves model performance. The DS4 dataset produced the lowest accuracy LAIe predictions (R^2 ≈0.24, RMSE ≈0.39). Graphically, it showed a weaker relationship between the observed values and the predictions compared to the other datasets (Figure 4). This indicates that the limitations in the spatial resolution and accuracy of satellite-based data reduce the accuracy of LAIe estimation. The DS5 dataset, created by combining all data sources, showed higher performance in LAIe prediction than the DS1, DS2, and DS4 datasets (R^2 ≈0.57, RMSE ≈0.30). As with DS3, these results show that integrating different data types can provide better predictions than individual datasets. In general, the findings indicate that UAV-based data, especially when combined (DS3), provide lower error values in LAIe prediction than S2 images. When Table 5 and Figure 5 are evaluated together, DS3 produced better LAIe predictions than all other datasets.

Significant differences in model performance were found between the datasets. The DS3 dataset had the lowest error values (RMSE% ≈24.4) and showed that the combined use of 2D orthomosaic derived spectral and SfM-derived 3D structural features from the UAV increased model accuracy (Table 5). The DS4 dataset produced the highest error values (RMSE% ≈32.1) and demonstrated lower performance in LAIe estimation compared to other datasets when using only satellite-based data. The DS1 (RMSE% ≈27.3) and DS2 (RMSE% ≈29.6) datasets produced medium-level error values, while the DS5 dataset (RMSE% ≈24.8) demonstrated that combining different data sources increased the model's predictive power, despite having slightly higher errors compared to DS3. The bias values obtained for all datasets were very close to zero (Table 5). However, such low mean bias values should be interpreted with caution. This is because these results do not indicate the absence of systematic error; instead, they may reflect a balance between overestimation and underestimation across the entire range of observations. Accordingly, the deviation was evaluated here not as a complete measure of prediction reliability, but as an indicator of the mean biased error. As shown in Figure 6, the residuals were

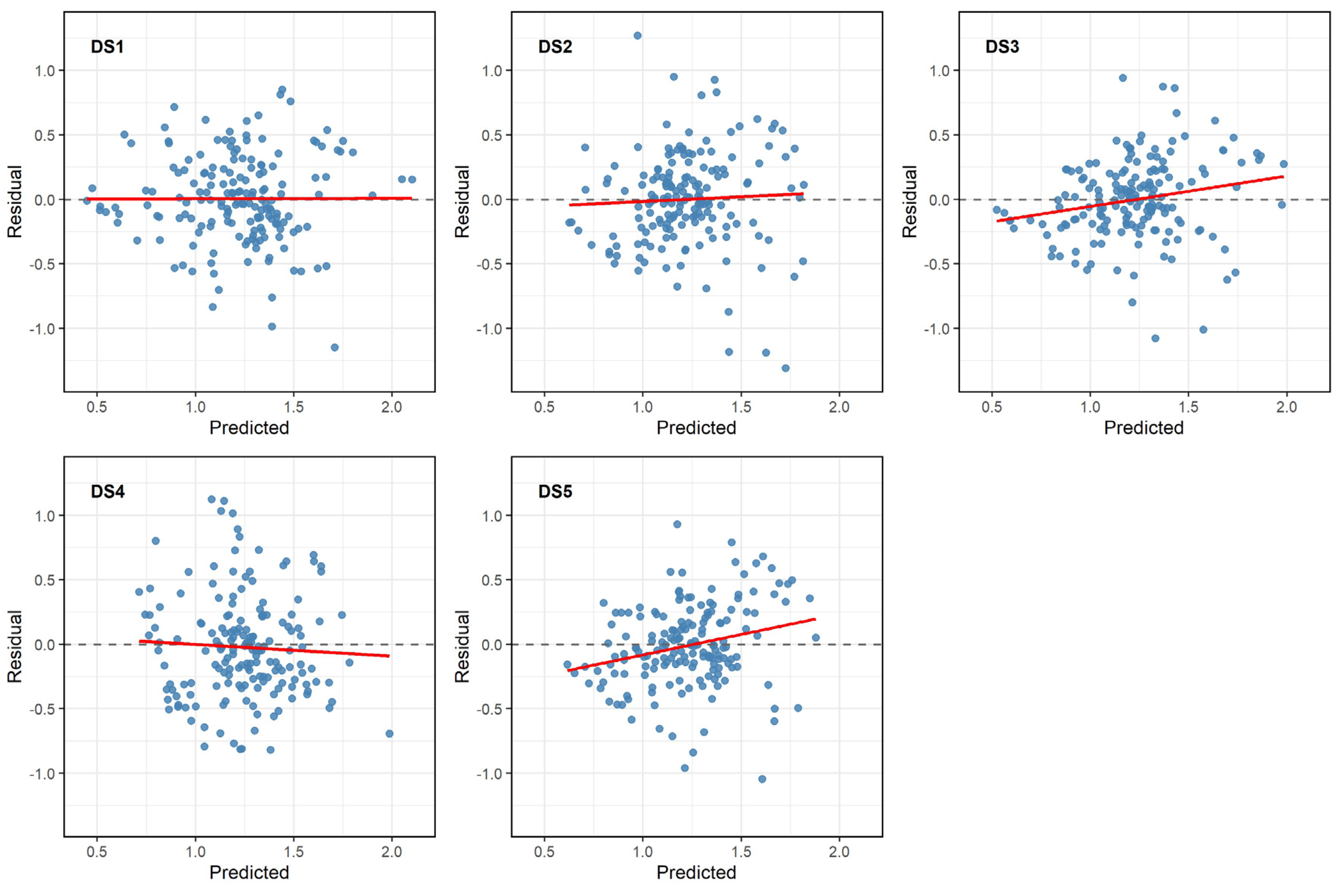

FIGURE 6 | Bias distributions corresponding to LAIe values predicted with different datasets (DS1–DS5). In this figure, Bias was defined as Observed − Predicted. Each panel shows the bias values plotted against the predicted LAIe values. The black dashed line represents the zero bias reference, while the red solid line indicates the linear trend of bias across the prediction range.

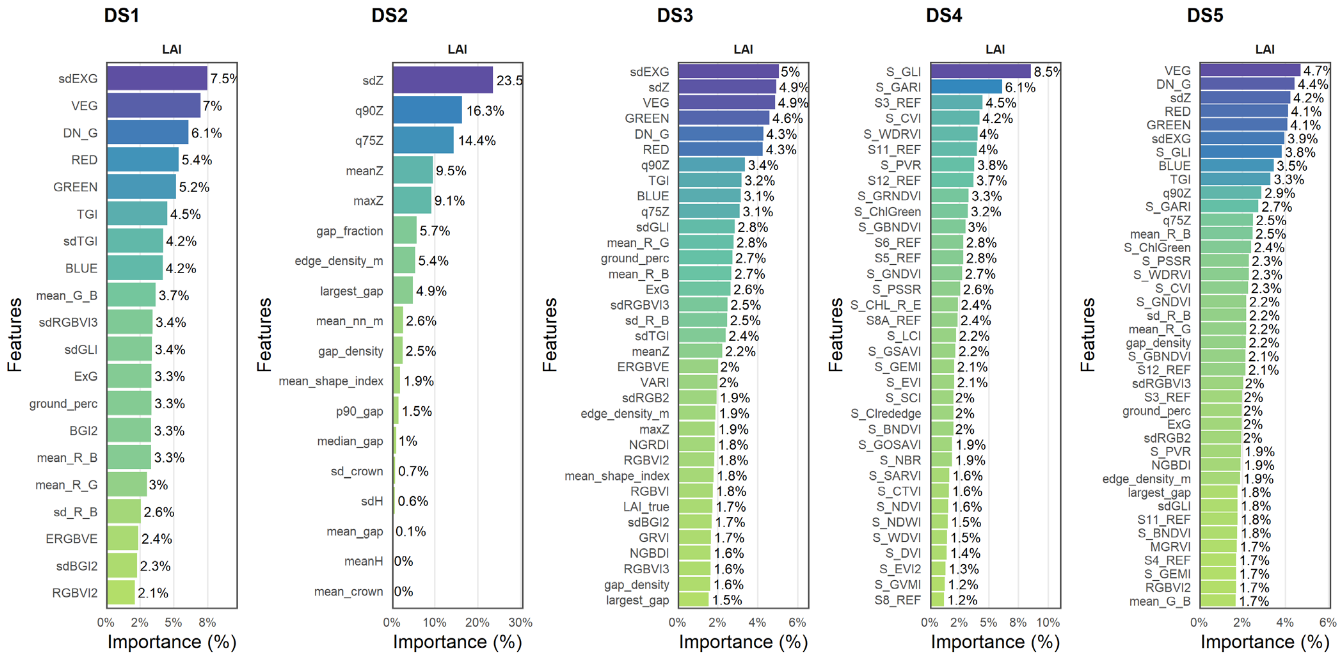

FIGURE 7 | Importance levels of features (DS1–DS5) obtained from UAV and S2 data in LAIe estimation.

generally distributed around zero, but slight trends specific to the dataset were also observed. This shows that the prediction errors may have varied along the LAIe gradient.

In the final stage, feature importance analyzes were performed to determine which features were most explanatory in LAIe estimation (Figure 7). The results revealed that the importance ranking varied across different data sources. In DS1, sdEXG (standard deviation of the Excess Green Index, 7.5%), VEG (Vegetation Index, 7%), and DN_G (digital value of the green band, 6.1%) were the most important features. The results indicate that UAV-based spectral characteristics, particularly those emphasizing green intensity and variability, play a strong explanatory role in LAIe prediction.

In the DS2 dataset, the statistical variables related to height sdZ (23.5%), q90Z (16.3%), and q75Z (14.4%) stood out as the most dominant variables. This result demonstrates that structural metrics derived from UAV point cloud data contribute significantly to LAIe estimation. In the DS3 dataset, where both spectral and structural variables were evaluated together, it was determined that both groups of variables contributed to the model at a similar level. In this context, it was observed that the importance levels of structural features such as sdEXG (5%) and sdZ (4.9%) were quite close to those of spectral features such as VEG (4.9%) and GREEN (4.6%). This indicates that the joint evaluation of both spectral and structural variables is important in LAIe estimation. In the DS4 dataset, derived solely from S2 data, S_GLI (8.5%), S_GARI (6.1%), and S_CVI (4.2%) were identified as the most significant prediction variables. This finding demonstrates that vegetation indices representing chlorophyll content and the greenness level of vegetation play a decisive role in satellite-based LAIe estimation. Finally, in the DS5 dataset, which combines UAV and S2 data, VEG (4.7%), DN_G (4.4%), sdZ (4.2%), and GREEN (4.1%) emerged as the most effective variables, while the S_GLI variable (3.8%) derived from S2 data was also found to make a significant contribution to the model.

4 | Discussion

In the study, the features sdEXG, VEG, DN_G, RED, and GREEN were the most important for LAIe prediction in the DS1 dataset (Figure 7). Green band weighted indicators such as VEG, DN_G, and GREEN are sensitive to chlorophyll. While an increase in chlorophyll increases shading absorption, this increase is often associated with an increase in LAI (Hunt et al. 2013). RGB plant indices such as sdEXG, on the other hand, externalize the canopy void dynamics associated with LAI by capturing ground plant separation and canopy cover (Du et al. 2022). Thus, it was expected that these features would be good explanatory features in LAIe prediction. In DS2, structural features such as sdZ, q90Z, q75Z, gap_fraction, and edge_gap_density appeared as significant features in the importance level graphs (Figure 7). Height features with high percentiles (q90Z, q75Z) and height variance (sdZ) were expected to be the most important features for LAIe, as they correspond to canopy closure and layering. The strong relationship between these types of percentile height indicators and LAI has been emphasized in the literature (Qu et al. 2018; Wang and Fang 2020). However, an important methodological limitation of the DS2 structural metrics should also be considered. In the present study, terrain normalization and the derivation of height-related variables were based on RGB photogrammetry using the SfM approach rather than LiDAR. Because surfaces visible in the imagery are only reconstructed by photogrammetric point clouds, ground detection under dense forest canopy may remain incomplete, which can introduce uncertainty into the DTM and, consequently, into canopy height normalization. This issue is particularly relevant for height-derived metrics such as sdZ, q90Z, and q75Z because any error in the estimated ground surface propagates directly into the distribution and percentile structure of normalized heights. LiDAR or ALS-based DTMs generally provide higher accuracy than SfM-based DTMs in forests due to better canopy penetration and lack of canopy shading effects. In contrast, it has been reported that UAV SfM accuracy tends to decrease under dense canopy cover and complex site conditions (Iglhaut et al. 2019; Dhruva et al. 2024; Hartley et al. 2025). Therefore, although the significant contribution of sdZ, q90Z, and q75Z to the LAIe estimate is ecologically meaningful, the low accuracy of the DTM used in the calculation of these variables, which is derived from SfM, constitutes a major limitation. This situation is thought to have potentially affected the strength of the relationship between structural predictor variables and LAIe.

In principle, features describing the amount of canopy gaps are directly related to LAIe, because they reflect the light transmittance and leaf density of the vegetation cover. Particularly in DS2 and partially in DS3, the meaningfulness of gap_fraction and gap_density is based on physical (morphological) causes. Gap_fraction (gap ratio) represents the proportion of light passing through the canopy structure, gap_density represents the distribution frequency of these gaps per unit area, and ground_percent represents the amount of light reaching the ground. An increase in these parameters indicates a decrease in leaf area density (Battuvshin and Menzel 2022; Sani-Mohammed et al. 2024). This relationship can be explained by the absorption and scattering mechanism of light passing through the vegetation cover, which forms the basis of Beer–Lambert's law. Indeed, as the void ratio decreases, an increase in the predicted LAI value is expected (Yan et al. 2019; Grotti et al. 2020). Therefore, these criteria are among the key determinants in predicting LAI using optical methods, and the fact that features describing the gap fractions were obtained as important features in LAI prediction was expected (Qu et al. 2018). Furthermore, the presence of sdEXG among the important features is explained by its relationship with crown heterogeneity and clumping signals, which vary along with LAI (Yan et al. 2019).

The DS3 dataset, which is the general UAV dataset composed of the combination of the DS1 and DS2 datasets, is the dataset that achieved the best prediction performance (Table 5). In DS3, the features sdEXG, sdZ, GREEN, VEG, DN_G, RED, and q90Z were among the most important features. This combination of pixel and point cloud -based features captures two different aspects of LAIe simultaneously. When the pigment/cover ratio (RGB-VIs) is combined with closure, gap, and layering (height features), limitations in one dataset (e.g., red band saturation or species-related variability) can be compensated by the strengths of the others, improving overall prediction accuracy. The clearly superior performance of the DS3 dataset compared to the individual datasets can be attributed to the complementary effect of combining morphological (height distributions, void ratios) and spectral features (RGB reflectance and indices). This is because spectral data provide information about plant pigmentation and canopy cover, while morphological features reflect the three-dimensional closure and heterogeneity of the canopy structure. Literature also shows that combining these two data types yields more accurate results than using spectral or structural data alone (Qiao et al. 2022; Jiang et al. 2023).

In the DS4 dataset derived from S2 data, green and chlorophyll focused features such as S_GLI, S_GARI, S3_REF (Green), and S_CVI were the most important features. However, this dataset also had the lowest LAIe prediction accuracy. In fact, this finding highlights the strengths of the RGB sensor equipped UAV compared to freely available S2 satellite imagery. S2's 10–20 m spatial resolution causes it to lose canopy gaps and fine scale heterogeneity, especially in rugged terrain. In contrast, the centimeter scale detail of the UAV provides more accurate results (Mangewa et al. 2022; Bulut et al. 2024). Another factor that may have contributed to the relatively poor performance of the DS4 dataset is the geometric mismatch between the locations of the field plots and the S2 pixels. In this study, while the radii of the sample plots ranged from approximately 11.28 to 15.96 m, the S2 predictor variables were derived from 10 m and 20 m pixels. Under these conditions, even relatively small positional uncertainties in plot coordinates can affect which satellite pixels the plot polygons intersect, particularly along forested edges or in structurally heterogeneous areas where the likelihood of mixed pixel effects is higher. Previous studies have shown that field parcel location errors can significantly affect parcel-level remote sensing models, and that correcting such errors can significantly reduce the RMSE (Jung et al. 2013). In addition, it has been emphasized that the scale mismatch between plot based LAIe measurements and coarser satellite pixels can be a significant source of uncertainty, particularly when vegetation exhibits significant heterogeneity at the sub pixel level (Revill et al. 2020). Therefore, in addition to the spectral saturation and spatial resolution limitations of S2, it is thought that the mismatch between the S2 pixel geometry and the deviation in the center positions of the GNSS based plots may have exacerbated the mixed-pixel issue by affecting the sample area overlap, thereby weakening the relationship between the S2 variables and the field measured LAIe in DS4. Therefore, in addition to the spectral saturation and spatial resolution limitations of S2, it is thought that the mismatch between the S2 pixel geometry and the deviation in the center positions of the GNSS based plots may have exacerbated the mixed-pixel issue by affecting the sample area overlap, thereby weakening the relationship between the S2 variables and the field measured LAIe in DS4. Furthermore, the fact that S2's red-NIR based vegetation indices reach saturation at medium high LAI levels and lose their sensitivity (Gitelson 2004) may also constrain the success of LAI prediction. Indeed, when S2's biophysical products such as LAIe are compared across different ecosystems, systematic underestimations occur particularly in forests (Fernandes et al. 2023; Putzenlechner et al. 2019). Another point to consider regarding the DS4 dataset is the potential impact of the atmospheric correction process applied to the S2 data on the predictor variables. In this study, L1C data containing Top of Atmosphere (TOA) reflectance values were converted to Bottom of Atmosphere (BOA) reflectance values using the SCP workflow (Congedo 2021). However, obtaining the BOA reflectance value is a critical preprocessing step for the reliable modeling of biophysical variables, and uncertainties arising at this stage may be reflected in vegetation indices and LAI modeling results (Main-Knorn et al. 2017). Additionally, it has been reported that differences in atmospheric correction algorithms and processing parameters can introduce significant variability in S2 surface reflectance products, which in turn can affect subsequent regression performance (Valdivieso-Ros et al. 2021). Therefore, in addition to the spatial resolution and spectral saturation limitations of the S2 data, it is considered that residual uncertainties in the process of deriving the BOA reflectance value from the L1C data may also have contributed to the relatively low performance of the DS4 dataset.

While access to S2 satellite imagery is free and offers advantages in LAIe estimation in large-scale studies, low-cost RGB sensor equipped UAVs can provide more accurate results in smaller or medium scale due to their high spatial resolution, temporal flexibility, and ability to collect data on site (Zhao et al. 2022; Vélez et al. 2023). UAVs can perform flights at the desired time and location, enabling simultaneous data collection with field measurements. Furthermore, structural and spectral information about vegetation cover can be obtained. Our results showed that UAVs offer lower error and deviation values in LAIe estimation, making them reliable in applications such as monitoring plant health, determining water stress, mapping disease intensity, and optimizing yield estimation. However, satellite platforms such as S2 remain an indispensable tool in national or regional scale studies. Therefore, these two approaches should be considered as complementary observation systems at different spatial scales (Li et al. 2022; Vélez et al. 2023).

Finally, the results of the DS5 dataset, created from the combination of all datasets, showed that the explanatory features important for LAIe prediction (Figure 7) were predominantly obtained from UAV data (DN_G, sdZ, VEG, GREEN, S_GLI, sdEXG). DS5 was the most successful prediction dataset for LAIe estimation after DS3. Although DS5 exhibited slightly lower performance than DS3 (Table 5), this difference is considered to result from minor randomness in the RF predictions. Nevertheless, integrating all data sources provided competitive and, in some cases, even superior prediction performance compared to using individual datasets. Despite the satisfactory results obtained in LAIe prediction, several factors are considered to have influenced the relatively moderate model accuracies. It has been reported that the level of positional accuracy in UAV imagery can reduce prediction accuracy, particularly in forest structures that exhibit high spatial variability over short distances (Puliti et al. 2015). In addition, minor errors in the DTM may propagate into height-based variables such as canopy height percentiles or gap ratios, thereby affecting their relationship with LAI (Lin et al. 2020). Furthermore, this situation may depend not only on the modeling approach but also on the method used to derive the ground-based LAIe data employed as reference values. Minor errors in the thresholding parameters used during hemispherical photograph analysis may lead to classification errors and uncertainty in the separation of shaded and gap areas, which in turn may cause inconsistencies between observed and estimated values (Beckschäfer et al. 2013). As an addition, changes in weather conditions and skylight during image acquisition can affect the interpretation of hemispheric photographs, thereby introducing additional uncertainty into LAIe estimates. It has been reported that light-to-dark ratio estimates based on hemispheric photographs can be particularly affected by variable sky illumination and exposure conditions. This, in turn, can cause deviations in light to dark ratio and consequently in LAI calculations (Visscher von Arx et al. 2007). In addition, it is well known that optical methods based on hemispherical imaging may systematically underestimate actual LAIe values, particularly in coniferous forests, due to needle clumping and the non-uniform distribution of plant elements (Chen and Black 1992; Jonckheere et al. 2004). Since no explicit clumping correction was applied in the present study, the reference variable used corresponds to LAI, and the uncertainties associated with optical measurement were therefore directly inherited by the model training data. Therefore, it is considered that uncertainties related to image acquisition conditions, along with the thresholding process, may be among the factors limiting the accuracy of the reference LAIe data and model performance. Similarly, the literature indicates that LAI estimates obtained using optical methods can directly influence model performance, and prediction errors may increase, particularly in low LAI ranges (Bréda 2003). All these factors together may explain why the obtained accuracy values were slightly lower than expected, despite the overall consistency of the results with the literature.

In general, the highest LAIe prediction accuracy in our study was achieved using the UAV_ALL dataset (DS3) (Table 5). Wang and Fang (2020) reported R^2 values between 0.58 and 0.65 for LAIe prediction using oblique UAV photogrammetry in forest ecosystems, and our DS3 result ($R^2 \approx 0.60$) falls within this range, indicating comparable performance. Moreover, the RMSE obtained in our study (≈0.30) was lower than the values commonly reported in similar studies (Table 5). Research using UAVs equipped with hyperspectral sensors has achieved higher prediction accuracy ($R^2 \approx 0.88$ and RMSE ≈0.20; Zhang et al. 2025), although these systems are considerably more expensive and operationally demanding. Likewise, Zhao et al. (2023) reported an R^2 of approximately 0.70 for LAI estimation in mangrove forests using the PROSAIL-D model and XGBoost. While these studies demonstrate superior or different levels of accuracy, it is important to note that variations in sensor types, forest structures, and LAI ranges can substantially influence model performance; therefore, direct comparisons of RMSE and R^2 values across studies should be interpreted with caution. These differences can largely be attributed to natural variability arising from the structural characteristics of different ecosystems. Forests with dense and homogeneous canopy structures exhibit more pronounced spectral heterogeneity due to the vertical stratification and trunk gaps typical of coniferous stands. Studies using ALS have reported that semi-physical and empirical models yield results in the range of $R^2 \approx 0.70–0.85$ (Zhang et al. 2024). The main reason is ALS sensor's ability to accurately reveal the three-dimensional canopy structure, which is directly related to LAI. Point clouds obtained from RGB cameras can also provide three-dimensional information about the canopy structure. However, ALS allows for more detailed modeling of lower canopy layers, thanks to the ability of laser pulses to penetrate different layers of vegetation. In this respect, ALS point clouds provide a more dense, accurate, and penetrative three-dimensional representation compared to UAV-based point clouds (Wang and Fang 2020). Furthermore, ALS offers the ability to collect data independently of sunlight or atmospheric conditions, thereby eliminating the effects of shading, cloud cover, or light changes that may be problematic with spectral images. Therefore, the ability of ALS data to directly capture structural metrics such as canopy density, void ratios, and height distributions may be the primary factor explaining its superior performance in LAI estimation.

5 | Conclusions

In this study, LAIe was estimated in pure Scots pine (*Pinus sylvestris* L.) stands using five different datasets derived from RGB sensor UAV data and S2 data. The findings indicated that the DS3 dataset, which combines UAV-based spectral variables with point cloud-based structural variables generated using the SfM approach, offered relatively higher prediction accuracy among the datasets examined ($R^2 \approx 0.60$; RMSE ≈ 0.30). Similarly, relatively high accuracy levels were also achieved with the DS5 dataset, which utilizes all data sources together. These results suggest that the combined use of spectral and structural variables derived from low-cost UAV systems equipped with RGB sensors may hold significant potential for LAIe estimation. Nevertheless, it is considered useful to take certain limitations into account when evaluating the study's findings. First, the reference LAIe data were obtained using the hemispheric photography technique, which is an optical method. Such methods can produce a certain degree of deviation from the actual LAIe value, particularly in coniferous stands, due to the inclusion of woody components in the image, the effect of needle clumping, and uncertainties associated with the image thresholding process. Therefore, reference data may have introduced a certain degree of uncertainty into the model training and validation process. In future research, if corrections for woody material and clustering effects are accounted for using devices that directly measure LAI, terrestrial LiDAR data, destructive measurements, or species-specific allometric equations, the reference LAIe data could better represent the actual leaf area, and consequently, model performance could be evaluated more accurately.

Secondly, both UAV and S2 data were used as if they were from a single point in time. This results in the developed models primarily reflecting the structural and spectral conditions present at the time of measurement. However, it is known that LAIe can exhibit temporal variations depending on phenological development, climatic variability, and interannual environmental differences. Therefore, it is assessed that the use of multi-temporal UAV and satellite data in the future could allow for a more detailed monitoring of seasonal and interannual LAIe dynamics, which could significantly contribute to the temporal validity of the models and LAIe prediction.

Thirdly, this study utilized only RGB sensor data, and three-dimensional structural information was derived from photogrammetric point clouds generated using the SfM approach rather than direct active remote sensing systems. While RGB-based photogrammetric data is considered to offer significant advantages in terms of low cost, accessibility, and operational feasibility, it is assessed that it may have certain limitations, particularly regarding the representation of lower canopy levels, the resolution of vertical structure in densely forested areas, and the mitigation of shadow effects. Therefore, it is anticipated that further improvements in model accuracy could be achieved by jointly analyzing multispectral, hyperspectral, or LiDAR-based data alongside RGB-based variables, as this would allow for a more comprehensive representation of both spectral and structural information.

Finally, the developed models were applied only to natural pure Scots pine stands, and remote sensing data were collected during a single period (September). Therefore, the relationships identified reflect the crown structure of a specific species and a specific phenological stage. While this constitutes another limitation of our study, it is believed that this may restrict the direct generalization of the findings to mixed stands, deciduous forest communities, different phenological stages, different ecological conditions, and different geographic regions. Although the highest model performance was achieved with the DS3 dataset ($R^2 \approx 0.60$), it is observed that a significant amount of variance remains unexplained. Additionally, since model performance was evaluated using a 10-fold random cross-validation method and no independent test set was used, the reported accuracy metrics may have been slightly overestimated if spatial autocorrelation existed among geographically close sample plots. However, this potential source of bias may have been partly limited by the sampling design, as the plots were established to represent different stand ages, crown closure classes, and site conditions rather than being concentrated as multiple closely spaced plots within the same stand. This is considered an indication that the transferability of the developed model structure across different species, stand structures, and seasonal conditions has not yet been fully established. Therefore, it is anticipated that the model's generalizability could be evaluated more comprehensively if similar modeling approaches are tested in the future using mixed stands, different forest types (deciduous and coniferous), varying elevation and slope conditions, different ecological regions, and multi-temporal datasets.

In general, the study demonstrates that the combined use of spectral and structural variables derived from UAV RGB imagery can be a practical and operationally flexible option, particularly in situations requiring high spatial detail and site-specific data collection. In cases where higher cost data sources, such as ALS or commercial very high-resolution imagery, are not available, UAV RGB data has been shown to be an accessible alternative for obtaining both spectral and photogrammetric structural information at the plot level.

Acknowledgments

This study was also conducted during the author Hasan Aksoy's tenure as a visiting scientist at the Finnish Natural Resources Institute (LUKE) under the Tübitak 2219 Postdoctoral Research Fellowship program (Grant No: 1059B192302166). Author Hasan Aksoy expresses his gratitude for the support provided by TÜBİTAK. The authors would like to thank the Institute of Natural and Applied Science and Scientific Research Project Unit of Çankırı Karatekin University, Turkey.

Funding

This research was supported by the Institute of Natural and Applied Sciences and the Scientific Research Project Unit (Grant No: OF211221D08) at Çankırı Karatekin University in Turkey during the collection of field data. Open access publication support is provided through the TÜBİTAK—Wiley Open Access Agreement.

Conflicts of Interest

The authors declare no conflicts of interest.

Data Availability Statement

The datasets used in this study can be accessed at the following on Mendeley Data: https://data.mendeley.com/preview/7gthb4hhct?a=fb69272e-9def-4d2c-a339-a310505e8099 (Aksoy 2026).

References

Aksoy, H. 2022. "Sinop Orman Bölge Müdürlüğü saf Sarıçam Meşcerelerinde Farklı Uzaktan Algılama Verileri Kullanılarak Bazı

Meşcere Parametrelerinin Modellenmesi." Doctoral dissertation, Doktora Tezi, Çankırı Karatekin Üniversitesi, 160 sayfa, Çankırı.

Aksoy, H. 2024. "Estimation Stand Volume, Basal Area and Quadratic Mean Diameter Using Landsat 8 OLI and Sentinel-2 Satellite Image With Different Machine Learning Techniques." *Transactions in GIS* 28, no. 8: 2687–2704. https://doi.org/10.1111/tgis.13265.

Aksoy, H. 2026. "Prediction of LAI in Scots Pine Forests of Türkiye Using UAV and Sentinel 2 Images." *Mendeley Data* V3. https://doi.org/10.17632/7gthb4hhct.3.

Aksoy, H., and A. Günlü. 2025a. "Estimation of Aboveground Carbon Using Different Remote Sensing Data and Modelling Techniques." *Kastamonu University Journal of Forestry Faculty* 25, no. 2: 152–176. https://doi.org/10.17475/kastorman.1787120.

Aksoy, H., and A. Günlü. 2025b. "UAV and Satellite-Based Prediction of Aboveground Biomass in Scots Pine Stands: A Comparative Analysis of Regression and Neural Network Approaches." *Earth Science Informatics* 18, no. 1: 66. https://doi.org/10.1007/s12145-024-01657-0.

Battuvshin, G., and L. Menzel. 2022. "Adjusting Line Quantum Sensing to Improve Leaf Area Index Measurements and Estimations in Forests." *MethodsX* 9: 101805. https://doi.org/10.1016/j.mex.2022.101805.

Beckschäfer, P., D. Seidel, C. Kleinn, and J. Xu. 2013. "On the Exposure of Hemispherical Photographs in Forests." *iForest - Biogeosciences and Forestry* 6, no. 4: 228–237. https://doi.org/10.3832/ifor0957-006.

Bendig, J., K. Yu, H. Aasen, et al. 2015. "Combining UAV-Based Plant Height From Crop Surface Models, Visible, and Near Infrared Vegetation Indices for Biomass Monitoring in Barley." *International Journal of Applied Earth Observation and Geoinformation* 39: 79–87. https://doi.org/10.1016/j.jag.2015.02.012.

Bhattarai, R., P. Rahimzadeh-Bajgiran, A. Weiskittel, S. Homayouni, T. W. Gara, and R. P. Hanavan. 2022. "Estimating Species-Specific Leaf Area Index and Basal Area Using Optical and SAR Remote Sensing Data in Acadian Mixed Spruce-Fir Forests, USA." *International Journal of Applied Earth Observation and Geoinformation* 108: 102727. https://doi.org/10.1016/j.jag.2022.102727.

Birth, G. S., and G. R. McVey. 1968. "Measuring the Color of Growing Turf With a Reflectance Spectrophotometer 1." *Agronomy Journal* 60, no. 6: 640–643.

Blackburn, G. A. 1998. "Spectral Indices for Estimating Photosynthetic Pigment Concentrations: A Test Using Senescent Tree Leaves." *International Journal of Remote Sensing* 19, no. 4: 657–675.

Bréda, N. J. 2003. "Ground-Based Measurements of Leaf Area Index: A Review of Methods, Instruments and Current Controversies." *Journal of Experimental Botany* 54, no. 392: 2403–2417. https://doi.org/10.1093/jxb/erg263.

Breiman, L. 2001. "Random Forests." *Machine Learning* 45, no. 1: 5–32. https://doi.org/10.1023/A:1010933404324.

Bulut, S., A. Günlü, H. Aksoy, F. Bolat, and M. Y. Sönmez. 2024. "Integration of Field Measurements With Unmanned Aerial Vehicle to Predict Forest Inventory Metrics at Tree and Stand Scales in Natural Pure Crimean Pine Forests." *International Journal of Remote Sensing* 45, no. 12: 3846–3870. https://doi.org/10.1080/01431161.2024.2357837.

Chen, J. M., and T. A. Black. 1992. "Defining Leaf Area Index for Non-Flat Leaves." *Plant, Cell & Environment* 15, no. 4: 421–429. https://doi.org/10.1111/j.1365-3040.1992.tb00992.x.

Chen, J. M., and J. Cihlar. 1996. "Retrieving Leaf Area Index of Boreal Conifer Forests Using Landsat TM Images." *Remote Sensing of Environment* 55, no. 2: 153–162. https://doi.org/10.1016/0034-4257(95)00195-6.

Congedo, L. 2021. "Semi-Automatic Classification Plugin: A Python Tool for the Download and Processing of Remote Sensing Images in QGIS." *Journal of Open Source Software* 6, no. 64: 3172.

Crippen, R. E. 1990. "Calculating the Vegetation Index Faster." *Remote Sensing of Environment* 34: 71–73.

Dalponte, M., and D. A. Coomes. 2016. "Tree-Centric Mapping of Forest Carbon Density From Airborne Laser Scanning and Hyperspectral Data." *Methods in Ecology and Evolution* 7, no. 10: 1236–1245. https://doi.org/10.1111/2041-210X.12575.

Delta-T Devices. n.d. "HemiView User Manual (HemiView 2.1 SR4) Dynamax." https://dynamax.com/images/uploads/papers/HemiView_Manual.pdf.

DeVries, B., A. K. Pratihast, J. Verbesselt, L. Kooistra, and M. Herold. 2016. "Characterizing Forest Change Using Com-Munity-Based Monitoring Data and Landsat Time Series." *PLoS One* 11, no. 3: e0147121.

Dhruva, A., R. J. Hartley, T. A. Redpath, H. J. C. Estarija, D. Cajes, and P. D. Massam. 2024. "Effective UAV Photogrammetry for Forest Management: New Insights on Side Overlap and Flight Parameters." *Forests* 15, no. 12: 2135. https://doi.org/10.3390/f15122135.

Du, L., H. Yang, X. Song, et al. 2022. "Estimating Leaf Area Index of Maize Using UAV-Based Digital Imagery and Machine Learning Methods." *Scientific Reports* 12, no. 1: 15937. https://doi.org/10.1038/s41598-022-20299-0.

Du, M., and N. Noguchi. 2017. "Monitoring of Wheat Growth Status and Mapping of Wheat Yield's Within-Field Spatial Variations Using Color Images Acquired From UAV-Camera System." *Remote Sensing* 9, no. 3: 289. https://doi.org/10.3390/rs9030289.

ESA. 2022. "Website." https://scihub.copernicus.eu/.

Fang, H., S. Liang, J. R. Townshend, and R. E. Dickinson. 2008. "Spatially and Temporally Continuous LAI Data Sets Based on an Integrated Filtering Method: Examples From North America." *Remote Sensing of Environment* 112, no. 1: 75–93. https://doi.org/10.1016/j.rse.2006.07.026.

Fernandes, R., L. Brown, F. Canisius, et al. 2023. "Validation of Simplified Level 2 Prototype Processor Sentinel-2 Fraction of Canopy Cover, Fraction of Absorbed Photosynthetically Active Radiation and Leaf Area Index Products Over North American Forests." *Remote Sensing of Environment* 293: 113600. https://doi.org/10.1016/j.rse.2023.113600.

Frazier, R. J., N. C. Coops, and M. A. Wulder. 2015. "Boreal Shield Forest Disturbance and Recovery Trends Using Landsat Time Series." *Remote Sensing of Environment* 170: 317–327.

Gamon, J. A., and J. S. Surfus. 1999. "Assessing Leaf Pigment Content and Activity With a Reflectometer." *New Phytologist* 143, no. 1: 105–117.

García-Fernández, M., E. Sanz-Ablanedo, and J. R. Rodríguez-Pérez. 2021. "High-Resolution Drone-Acquired RGB Imagery to Estimate Spatial Grape Quality Variability." *Agronomy* 11, no. 4: 655. https://doi.org/10.3390/agronomy11040655.

Garrigues, S., R. Lacaze, F. J. T. M. Baret, et al. 2008. "Validation and Intercomparison of Global Leaf Area Index Products Derived From Remote Sensing Data." *Journal of Geophysical Research – Biogeosciences* 113, no. G2: 2007JG000635. https://doi.org/10.1029/2007JG000635.

GDF. 2022. *Sinop Regional Directorate of Forestry, Forest Planing Units, Forest Management Plans*. Republic of Turkey, General Directorate of Forestry, Forest Administration and Planning Department.

Gitelson, A. A. 2004. "Wide Dynamic Range Vegetation Index for Remote Quantification of Biophysical Characteristics of Vegetation." *Journal of Plant Physiology* 161, no. 2: 165–173. https://doi.org/10.1078/0176-1617-01176.

Gitelson, A. A., U. Gritz, and M. N. Merzlyak. 2003. "Relationships Between Leaf Chlorophyll Content and Spectral Reflec-Tance and Algorithms for Non-Destructive Chlorophyll Assessment in Higher Plant Leaves." *Journal of Plant Physiology* 160, no. 3: 271–282.

Gitelson, A. A., Y. J. Kaufman, R. Stark, and D. Rundquist. 2002. "Novel Algorithms for Remote Estimation of Vegetation Fraction." *Remote Sensing of Environment* 80, no. 1: 76–87. https://doi.org/10.1016/S0034-4257(01)00289-9.

Gower, S. T., C. J. Kucharik, and J. M. Norman. 1999. "Direct and Indirect Estimation of Leaf Area Index, fAPAR, and Net Primary Production of Terrestrial Ecosystems." *Remote Sensing of Environment* 70, no. 1: 29–51. https://doi.org/10.1016/S0034-4257(99)00056-5.

Gower, S. T., and J. M. Norman. 1991. "Rapid Estimation of Leaf Area Index in Conifer and Broad-Leaf Plantations." *Ecology* 72, no. 5: 1896–1900. https://doi.org/10.2307/1940988.

Grotti, M., K. Calders, N. Origo, et al. 2020. "An Intensity, Image-Based Method to Estimate Gap Fraction, Canopy Openness and Effective Leaf Area Index From Phase-Shift Terrestrial Laser Scanning." *Agricultural and Forest Meteorology* 280: 107766. https://doi.org/10.1016/j.agrformet.2019.107766.

Günlü, A., S. Keleş, İ. Ercanlı, and M. Şenyurt. 2017. "Estimation of Leaf Area Index Using WorldView-2 and Aster Satellite Image: A Case Study From Turkey." *Environmental Monitoring and Assessment* 189, no. 11: 538. https://doi.org/10.1007/s10661-017-6254-2.

Hague, T., N. D. Tillett, and H. Wheeler. 2006. "Automated Crop and Weed Monitoring in Widely Spaced Cereals." *Precision Agriculture* 7: 21–32. https://doi.org/10.1007/s11119-005-6787-1.

Hardisky, M. A., V. Klemas, and R. M. Smart. 1983. "The Influence of Soil Salinity, Growth Form, and Leaf Moisture on the Spectral Radiance of *Spartina alterniflora* Canopies." *Photogrammetric Engineering and Remote Sensing* 49: 77–83.

Hartley, R. J., S. Jayathunga, J. S. Elleouet, B. S. Steer, and M. S. Watt. 2025. "UAV-Enabled Evaluation of Forestry Plantations: A Comprehensive Assessment of Laser Scanning and Photogrammetric Approaches." *Science of Remote Sensing* 12: 100245. https://doi.org/10.1016/j.srs.2025.100245.

Heiskanen, J., L. Korhonen, J. Hietanen, and P. K. Pellikka. 2015. "Use of Airborne Lidar for Estimating Canopy Gap Fraction and Leaf Area Index of Tropical Montane Forests." *International Journal of Remote Sensing* 36, no. 10: 2569–2583. https://doi.org/10.1080/01431161.2015.1041177.

Hijmans, R. J. 2018. "raster: Geographic Data Analysis and Modeling." R package version, 2, 8.

Huete, A. R. 1988. "A Soil Adjusted Vegetation Index (SAVI)." *Remote Sensing of Environment* 25: 295–309.

Hunt, E. R., Jr., P. C. Doraiswamy, J. E. McMurtrey, C. S. Daughtry, E. M. Perry, and B. Akhmedov. 2013. "A Visible Band Index for Remote Sensing Leaf Chlorophyll Content at the Canopy Scale." *International Journal of Applied Earth Observation and Geoinformation* 21: 103–112.

Iglhaut, J., C. Cabo, S. Puliti, L. Piermattei, J. O'Connor, and J. Rosette. 2019. "Structure From Motion Photogrammetry in Forestry: A Review." *Current Forestry Reports* 5, no. 3: 155–168. https://doi.org/10.1007/s40725-019-00094-3.

Janitza, S., and R. Hornung. 2018. "On the Overestimation of Random Forest's Out-Of-Bag Error." *PLoS One* 13, no. 8: e0201904. https://doi.org/10.1371/journal.pone.0201904.

Jensen, J. L., K. S. Humes, L. A. Vierling, and A. T. Hudak. 2008. "Discrete Return Lidar-Based Prediction of Leaf Area Index in Two Conifer Forests." *Remote Sensing of Environment* 112, no. 10: 3947–3957. https://doi.org/10.1016/j.rse.2008.07.001.

Jiang, J., P. M. Atkinson, C. Chen, et al. 2023. "Combining UAV and Sentinel-2 Satellite Multi-Spectral Images to Diagnose Crop Growth and N Status in Winter Wheat at the County Scale." *Field Crops Research* 294: 108860. https://doi.org/10.1016/j.fcr.2023.108860.

Jonckheere, I., S. Fleck, K. Nackaerts, et al. 2004. "Review of Methods for In Situ Leaf Area Index Determination: Part I. Theories, Sensors and Hemispherical Photography." *Agricultural and Forest Meteorology* 121, no. 1–2: 19–35. https://doi.org/10.1016/j.agrformet.2003.08.027.

Jung, J., S. Kim, S. Hong, et al. 2013. "Effects of National Forest Inventory Plot Location Error on Forest Carbon Stock Estimation Using k-Nearest Neighbor Algorithm." *ISPRS Journal of Photogrammetry and Remote Sensing* 81: 82–92. https://doi.org/10.1016/j.isprsjprs.2013.04.008.

Kalinowski, A., and S. Oliver. 2004. *ASTER Mineral Index Processing Manual*, 36. Remote Sensing Applications, Geoscience Australia.

Kaufman, Y. J., and D. Tanre. 1992. "Atmospherically Resistant Vegetation Index (ARVI) for EOS-MODIS." *IEEE Transactions on Geoscience and Remote Sensing* 30, no. 2: 261–270.

Key, C. H., and N. C. Benson. 2006. "Landscape Assessment (LA). FIREMON: Fire Effects Monitoring and Inventory System." 164: LA-1.

Khan, N. M., V. V. Rastoskuev, Y. Sato, and S. Shiozawa. 2005. "Assessment of Hydrosaline Land Degradation by Using a Simple Approach of Remote Sensing Indicators." *Agricultural Water Management* 77, no. 1–3: 96–109.

Li, M., R. R. Shamshiri, C. Weltzien, and M. Schirrmann. 2022. "Crop Monitoring Using Sentinel-2 and UAV Multispectral Imagery: A Comparison Case Study in Northeastern Germany." *Remote Sensing* 14, no. 17: 4426. https://doi.org/10.3390/rs14174426.

Li, S., and X. Chen. 2014. "A New Bare-Soıl Index for Rapid Mapping Developing Areas Using Landsat 8 Data." *ISPRS Annals of the Photogrammetry, Remote Sensing and Spatial Information Sciences* 2, no. 40: 139–144.

Liaw, A., and M. Wiener. 2002. "Classification and Regression by RandomForest." *R News* 2, no. 3: 18–22. https://journal.r-project.org/articles.

Lidar, A. 2002. "Lidar Remote Sensing for Ecosystem Studies." *Bioscience* 52, no. 1: 19–30. https://andrewsforest.oregonstate.edu/sites/default/files/lter/pubs/pdf/pub2813.pdf.

Lin, L., K. Yu, X. Yao, et al. 2021. "UAV Based Estimation of Forest Leaf Area Index (LAI) Through Oblique Photogrammetry." *Remote Sensing* 13, no. 4: 803. https://doi.org/10.3390/rs13040803.

Lin, X., M. Xu, C. Cao, et al. 2020. "Estimates of Forest Canopy Height Using a Combination of ICESat-2/ATLAS Data and Stereo-Photogrammetry." *Remote Sensing* 12, no. 21: 3649. https://doi.org/10.3390/rs12213649.

Liu, H. Q., and A. Huete. 1995. "A Feedback Based Modification of the NDVI to Minimize Canopy Background and Atmospheric Noise." *IEEE Transactions on Geoscience and Remote Sensing* 33, no. 2: 457–465.

Liu, Z., J. M. Chen, G. Jin, and Y. Qi. 2015. "Estimating Seasonal Variations of Leaf Area Index Using Litterfall Collection and Optical Methods in Four Mixed Evergreen–Deciduous Forests." *Agricultural and Forest Meteorology* 209: 36–48. https://doi.org/10.1016/j.agrformet.2015.04.025.

Louhaichi, M., M. M. Borman, and D. E. Johnson. 2001. "Spatially Located Platform and Aerial Photography for Documentation of Grazing Impacts on Wheat." *Geocarto International* 16, no. 1: 65–70. https://doi.org/10.1080/10106040108542184.

Lu, D., P. Mausel, E. Brondizio, and E. Moran. 2004. "Relationships Between Forest Stand Parameters and Landsat TM Spectral Responses in the Brazilian Amazon Basin." *Forest Ecology and Management* 198, no. 1–3: 149–167.

Main-Knorn, M., B. Pflug, J. Louis, V. Debaecker, U. Müller-Wilm, and F. Gascon. 2017. "Sen2Cor for Sentinel-2." In *Image and Signal Processing for Remote Sensing XXIII*, vol. 10427, 37–48. SPIE. https://doi.org/10.1117/12.2278218.

Mangewa, L. J., P. A. Ndakidemi, R. D. Alward, et al. 2022. "Comparative Assessment of UAV and Sentinel-2 NDVI and GNDVI for Preliminary

Diagnosis of Habitat Conditions in Burunge Wildlife Management Area, Tanzania." *Earth* 3, no. 3: 769–787. https://doi.org/10.3390/earth3030044.

Meyer, L. H., M. Heurich, B. Beudert, J. Premier, and D. Pflugmacher. 2019. "Comparison of Landsat-8 and Sentinel-2 Data for Estimation of Leaf Area Index in Temperate Forests." *Remote Sensing* 11, no. 10: 1160. https://doi.org/10.3390/rs11101160.

Mukherjee, N. R., and C. Samuel. 2016. "Assessment of the Temporal Variations of Surface Water Bodies in and Around Chennai Using Landsat Imagery." *Indian Journal of Science and Technology* 9, no. 18: 1–7.

Myneni, R. B., R. Ramakrishna, R. O. E. N. T. G. E. N. Nemani, and S. W. Running. 1997. "Estimation of Global Leaf Area Index and Absorbed PAR Using Radiative Transfer Models." *IEEE Transactions on Geoscience and Remote Sensing* 35, no. 6: 1380–1393. https://doi.org/10.1109/36.649788.

Niederheiser, R., M. Mokros, J. Lange, H. Petschko, G. Prasicek, and S. Oude Elberink. 2016. "Deriving 3D Point Clouds From Terrestrial Photographs Comparison of Different Sensors and Software." In *23rd Congress of the International Society of Photogrammetry and Remote Sensing: From Human History to the Future with Spatial Information* (pp. 685-692). http://www.isprs-ann-photogramm-remote-sens-spatial-inf-sci.net/III-2/.

Nilson, T. 1971. "A Theoretical Analysis of the Frequency of Gaps in Plant Stands." *Agricultural Meteorology* 8: 25–38. https://doi.org/10.1016/0002-1571(71)90092-6.

Omer, G., O. Mutanga, E. M. Abdel-Rahman, and E. Adam. 2016. "Empirical Prediction of Leaf Area Index (LAI) of Endangered Tree Species in Intact and Fragmented Indigenous Forests Ecosystems Using WorldView-2 Data and Two Robust Machine Learning Algorithms." *Remote Sensing* 8, no. 4: 324. https://doi.org/10.3390/rs8040324.

Pebesma, E., and R. S. Bivand. 2005. "S Classes and Methods for Spatial Data: The sp Package." *R News* 5, no. 2: 9–13.

Penuelas, J., F. Baret, and I. Filella. 1995. "Semi-Empirical Indices to Assess Carotenoids/Chlorophyll a Ratio From Leaf Spectral Reflectance." *Photosynthetica* 31, no. 2: 221–230.

Pix4D. 2024. "Dense Point Cloud – PIX4Dmatic." Pix4D Documentation. https://support.pix4d.com/hc/en-us/articles/360044439272.

Pope, G., and P. Treitz. 2013. "Leaf Area Index (LAI) Estimation in Boreal Mixedwood Forest of Ontario, Canada Using Light Detection and Ranging (LiDAR) and WorldView-2 Imagery." *Remote Sensing* 5, no. 10: 5040–5063. https://doi.org/10.3390/rs5105040.

Probst, P., M. N. Wright, and A. L. Boulesteix. 2019. "Hyperparameters and Tuning Strategies for Random Forest." *Wiley Interdisciplinary Reviews: Data Mining and Knowledge Discovery* 9, no. 3: e1301. https://doi.org/10.1002/widm.1301.

Puliti, S., J. Breidenbach, and R. Astrup. 2020. "Estimation of Forest Growing Stock Volume With UAV Laser Scanning Data: Can It Be Done Without Field Data?" *Remote Sensing* 12, no. 8: 1245. https://doi.org/10.3390/rs12081245.

Puliti, S., H. O. Ørka, T. Gobakken, and E. Næsset. 2015. "Inventory of Small Forest Areas Using an Unmanned Aerial System." *Remote Sensing* 7, no. 8: 9632–9654. https://doi.org/10.3390/rs70809632.

Putzenlechner, B., S. Castro, R. Kiese, et al. 2019. "Validation of Sentinel-2 fAPAR Products Using Ground Observations Across Three Forest Ecosystems." *Remote Sensing of Environment* 232: 111310. https://doi.org/10.1016/j.rse.2019.111310.

Qi, J., A. L. Chehbouni, A. R. Huete, Y. H. Kerr, and S. Sorooshian. 1994. "A Modified Soil Adjusted Vegetation Index (MSAVI)." *Remote Sensing of Environment* 48: 119–126.

Qiao, L., D. Gao, R. Zhao, et al. 2022. "Improving Estimation of LAI Dynamic by Fusion of Morphological and Vegetation Indices Based on UAV Imagery." *Computers and Electronics in Agriculture* 192: 106603. https://doi.org/10.1016/j.compag.2021.106603.

Qu, Y., A. Shaker, C. A. Silva, C. Klauberg, and E. R. Pinagé. 2018. "Remote Sensing of Leaf Area Index From LiDAR Height Percentile Metrics and Comparison With MODIS Product in a Selectively Logged Tropical Forest Area in Eastern Amazonia." *Remote Sensing* 10, no. 6: 970. https://doi.org/10.3390/rs10060970.

R Core Team. 2016. *R: A Language and Environment for Statistical Computing*. R Foundation for Statistical Computing. http://www.R-project.org/.

Revill, A., A. Florence, A. MacArthur, S. Hoad, R. Rees, and M. Williams. 2020. "Quantifying Uncertainty and Bridging the Scaling Gap in the Retrieval of Leaf Area Index by Coupling Sentinel-2 and UAV Observations." *Remote Sensing* 12, no. 11: 1843. https://doi.org/10.3390/rs12111843.

Richardson, J. J., L. M. Moskal, and S. H. Kim. 2009. "Modeling Approaches to Estimate Effective Leaf Area Index From Aerial Discrete-Return LIDAR." *Agricultural and Forest Meteorology* 149, no. 6–7: 1152–1160. https://doi.org/10.1016/j.agrformet.2009.02.007.

Rouse, J. W., R. H. Hass, J. A. Shell, and D. W. Deering. 1974. "Monitoring Vegetation Systems in the Great Plains With ERTS-l." *Proceedings, 3rd Earth Resources Technology Satellite Symposium* 1: 309–317.

Roussel, J. R., D. Auty, F. De Boissieu, and A. S. Meador. 2018. "lidR: Airborne LiDAR Data Manipulation and Visualization for Forestry Applications." R Package Version, 1(1).

Running, S. W., and J. C. Coughlan. 1988. "A General Model of Forest Ecosystem Processes for Regional Applications I. Hydrologic Balance, Canopy Gas Exchange and Primary Production Processes." *Ecological Modelling* 42, no. 2: 125–154. https://doi.org/10.1016/0304-3800(88)90112-3.

Sani-Mohammed, A., W. Yao, T. C. Wong, R. Fekry, and M. Heurich. 2024. "Characterizing Forest Plot Decay Levels Based on Leaf Area Index, Gap Fraction, and L-Moments From Airborne LiDAR." *Remote Sensing* 16, no. 15: 2824. https://doi.org/10.3390/rs16152824.

Schlerf, M., C. Atzberger, and J. Hill. 2005. "Remote Sensing of Forest Biophysical Variables Using HyMap Imaging Spectrometer Data." *Remote Sensing of Environment* 95, no. 2: 177–194.

Sellers, P. J., R. E. Dickinson, D. A. Randall, et al. 1997. "Modeling the Exchanges of Energy, Water, and Carbon Between Continents and the Atmosphere." *Science* 275, no. 5299: 502–509. https://doi.org/10.1126/science.275.5299.502.

Shao, Z., N. Yang, X. Xiao, L. Zhang, and Z. Peng. 2016. "A Multi-View Dense Point Cloud Generation Algorithm Based on Low-Altitude Remote Sensing Images." *Remote Sensing* 8, no. 5: 381. https://doi.org/10.3390/rs8050381.

Skidmore, A. K., N. C. Coops, E. Neinavaz, et al. 2021. "Priority List of Biodiversity Metrics to Observe From Space." *Nature Ecology & Evolution* 5, no. 7: 896–906. https://doi.org/10.1038/s41559-021-01595-w.

Sripada, R. P., R. W. Heiniger, J. G. White, and A. D. Meijer. 2006. "Aerial Color Infrared Photography for Determining Early in-Season Nitrogen Requirements in Corn." *Agronomy Journal* 98, no. 4: 968–977.

Themistocleous, K. 2019. "June DEM Modeling Using RGB-Based Vegetation Indices From UAV Images." In *Seventh International Conference on Remote Sensing and Geoinformation of the Environment (RSCy2019)*, vol. 11174, 499–506. SPIE. https://doi.org/10.1117/12.2532748.

Tucker, C. J. 1979. "Red and Photographic Infrared Linear Combinations for Monitoring Vegetation." *Remote Sensing of Environment* 8, no. 2: 127–150. https://doi.org/10.1016/0034-4257(79)90013-0.

Tucker, C. J. 1980. "A Spectral Method for Determining the Percentage of Green Herbage Material in Clipped Sample." *Remote Sensing of Environment* 9, no. 2: 175–181.

Vafaei, S., O. Fathizadeh, N. Puletti, H. Fadaei, S. Baqer Rasooli, and G. Vaglio Laurin. 2021. "Estimation of Forest Leaf Area Index Using Satellite Multispectral and Synthetic Aperture Radar Data in Iran." *iForest - Biogeosciences and Forestry* 14, no. 3: 278–284. https://doi.org/10.3832/ifor3633-014.

Valdivieso-Ros, C., F. Alonso-Sarria, and F. Gomariz-Castillo. 2021. "Effect of Different Atmospheric Correction Algorithms on Sentinel-2 Imagery Classification Accuracy in a Semiarid Mediterranean Area." *Remote Sensing* 13, no. 9: 1770. https://doi.org/10.3390/rs13091770.

Van Deventer, A. P., A. D. Ward, P. H. Gowda, and J. G. Lyon. 1997. "Using Thematic Mapper Data to Identify Contras-Ting Soil Plains and Tillage Practices." *Photogrammetric Engineering and Remote Sensing* 63: 87–93.

Vélez, S., M. Ariza-Sentís, and J. Valente. 2023. "Benchmarking the Reliability of Sentinel-2 Satellite Data for Estimating Vineyard NDVI and Leaf Area Index Parameters Through UAV LiDAR and Multispectral Imagery." *Environmental Sciences Proceedings* 29, no. 1: 1. https://doi.org/10.3390/ECRS2023-15859.

Verrelst, J., L. Alonso, G. Camps-Valls, J. Delegido, and J. Moreno. 2011. "Retrieval of Vegetation Biophysical Parameters Using Gaussian Process Techniques." *IEEE Transactions on Geoscience and Remote Sensing* 50, no. 5: 1832–1843. https://doi.org/10.1109/TGRS.2011.2168962.

Visscher von Arx, A., S. Huber, M. Kneubühler, and K. I. Itten. 2007. "Leaf Area Index Estimates Obtained for Mixed Forest Using Hemispherical Photography and HyMap Data." *Proceedings of the International Archives of the Photogrammetry, Remote Sensing and Spatial Information Sciences* XXXVI-7C50: 456–461.

Wallace, L., A. Lucieer, Z. Malenovský, D. Turner, and P. Vopěnka. 2016. "Assessment of Forest Structure Using Two UAV Techniques: A Comparison of Airborne Laser Scanning and Structure From Motion (SfM) Point Clouds." *Forests* 7, no. 3: 62. https://doi.org/10.3390/f7030062.

Wang, C., J. Chen, J. Wu, et al. 2017. "A Snow-Free Vegetation Index for Improved Monitoring of Vegetation Spring Green-Up Date in Deciduous Ecosystems." *Remote Sensing of Environment* 196: 1–12.

Wang, Y., and H. Fang. 2020. "Estimation of LAI With the LiDAR Technology: A Review." *Remote Sensing* 12, no. 20: 3457. https://doi.org/10.3390/rs12203457.

Welles, J. M., and J. M. Norman. 1991. "Instrument for Indirect Measurement of Canopy Architecture." *Agronomy Journal* 83, no. 5: 818–825. https://doi.org/10.2134/agronj1991.00021962008300050009x.

Woebbecke, D. M., G. E. Meyer, K. Von Bargen, and D. A. Mortensen. 1995. "Shape Features for Identifying Young Weeds Using Image Analysis." *Transactions of ASAE* 38, no. 1: 271–281.

Xie, R., R. Darvishzadeh, A. K. Skidmore, et al. 2021. "Mapping Leaf Area Index in a Mixed Temperate Forest Using Fenix Airborne Hyperspectral Data and Gaussian Processes Regression." *International Journal of Applied Earth Observation and Geoinformation* 95: 102242. https://doi.org/10.1016/j.jag.2020.102242.

Yan, G., R. Hu, J. Luo, et al. 2019. "Review of Indirect Optical Measurements of Leaf Area Index: Recent Advances, Challenges, and Perspectives." *Agricultural and Forest Meteorology* 265: 390–411.

Zarco-Tejada, P. J., A. Berjón, R. López-Lozano, et al. 2005. "Assessing Vineyard Condition With Hyperspectral Indices: Leaf and Canopy Reflectance Simulation in a Row-Structured Discontinuous Canopy." *Remote Sensing of Environment* 99, no. 3: 271–287. https://doi.org/10.1016/j.rse.2005.09.002.

Zhang, L., B. Zhang, H. Zhang, et al. 2025. "Multi-Source Feature Fusion Network for LAI Estimation From UAV Multispectral Imagery." *Agronomy* 15, no. 4: 988. https://doi.org/10.3390/agronomy15040988.

Zhang, S., L. Korhonen, M. Lang, et al. 2024. "Comparison of Semi-Physical and Empirical Models in the Estimation of Boreal Forest Leaf Area Index and Clumping With Airborne Laser Scanning Data." *IEEE Transactions on Geoscience and Remote Sensing* 62: 1–12. https://doi.org/10.1109/TGRS.2024.3353410.

Zhang, W., Z. Li, Y. Pu, et al. 2023. "Estimation of the Leaf Area Index of Winter Rapeseed Based on Hyperspectral and Machine Learning." *Sustainability* 15, no. 17: 12930. https://doi.org/10.3390/su151712930.

Zhao, D., J. Zhen, Y. Zhang, et al. 2023. "Mapping Mangrove Leaf Area Index (LAI) by Combining Remote Sensing Images With PROSAIL-D and XGBoost Methods." *Remote Sensing in Ecology and Conservation* 9, no. 3: 370–389. https://doi.org/10.1002/rse2.315.

Zhao, J., J. Yan, T. Xue, et al. 2022. "A Deep Learning Method for Oriented and Small Wheat Spike Detection (OSWSDet) in UAV Images." *Computers and Electronics in Agriculture* 198: 107087. https://doi.org/10.1016/j.compag.2022.107087.